Modeling of Thermal and Kinetic Processes in Non-Equilibrium Plasma Ignition Applied to a Lean Combustion Engine

Jacopo Zembi[1], Valentino Cruccolini[1], Francesco Mariani[1], Riccardo Scarcelli[2], Michele Battistoni[1]
1 Università degli Studi di Perugia, Department of Engineering, Italy
2 Argonne National Laboratory, United States of America

ABSTRACT

In recent years novel ignition systems have been developed to enable stable and efficient engine operations with lean mixtures. Among them, radio-frequency corona ignition systems create discharges that involve a much wider region compared to traditional spark, and produce non equilibrium plasma with high levels of active radicals and excited species. These devices considerably increase the early flame growth speed and extend stable operating limits. With the aim of expanding the knowledge on high efficiency lean-burn SI engines, this paper investigates and compares the combustion development generated by spark and corona ignitions through computational fluid dynamics, within the Reynolds-Averaged Navier-Stokes framework for turbulence modeling. In order to simultaneously take thermal and chemical effects into account, the Perfectly Stirred Reactor combustion model is used. Experimental data are also collected for validation in an optical access engine, for different mixture levels, from stoichiometric to very lean. The faster burn rate generated by the corona system in the initial stage of the combustion is well predicted by the simulations, in all the relative air-fuel ratio conditions. Remarkably, as the mixture becomes lean, simulations are able to capture the non-linear transition from fast to slow kernel growth, before a self-sustainable flame propagation is established. This correlates very well with the measured engine cyclic variability and the corresponding steep change in the duration of the flame kernel formation. Ultimately, this study highlights the important role of the atomic oxygen, as active radical, in promoting and enhancing the combustion initiated by a corona discharge, in addition to the volumetric ignition effect. By contrast, the validated simulations allow to explain that the high-temperature thermal plasma generated in a traditional spark discharge is insensitive to kinetic aspects.

INTRODUCTION

Current research effort to increase efficiency and reduce emissions has led to significant evolutions in spark ignition (SI) engines, such as the adoptions of boosting, cooled external exhaust gas recirculation, water injection and direct injection [1 - 12]. Beyond these technologies, the major research area towards clean and efficient internal combustion engines (ICEs) is still the quest for stable lean operation. As a matter of fact, lean combustion may cause excessive levels of cycle-to-cycle variability (CCV) or even misfires. These strategies are extremely challenging for the ignition system, which is requested to initiate a stable and repeatable combustion with small cyclic variation with very lean mixtures. Conventional spark plugs struggle at such unfavorable conditions. Therefore, alternative ignition systems are being developed to extend stable operating conditions to burn leaner mixtures than those achievable with traditional spark igniters [13, 14]. Multiple spark discharge [15 - 17], continuous discharge [18], high energy ignition systems [19 - 21] and pre-chamber turbulent jet ignition [22 - 24] can be considered upgrades of the conventional SI devices; these systems, based on the generation of thermal plasma [25 - 27], show some improvement in extending the engine stable limit, but still present some issues such as small ignition volume, heat losses through the electrodes [28], erosion and fouling.

A promising concept for internal combustion engine applications involves plasma-assisted ignition devices, such as RF corona discharge [29 - 32], nanosecond pulsed discharge [33 - 38], microwave assisted discharge [39 - 42] and dielectric barrier discharge [43 - 45]. The present work focuses on RF corona discharge, which produces a strong electric field at a frequency of about 1 MHz. The physical aspects that play a role on the corona discharge ignition can be identified in what follows:

1- Kinetic enhancement: active radicals and excited species produced by electron impacts in the plasma can be promoters of the ignition [46, 47].
2- Thermal enhancement: plasma increases temperature and accelerates chemical reactions and fuel oxidation according to the Arrhenius law.
3- Transport enhancement: the ionic wind and the hydrodynamic and Rayleigh instabilities produced by plasma change the local flow velocity and accelerate transition to turbulent regime and mixing [47 - 49].

The thermal effect is the predominant effect in all the equilibrium and near-equilibrium applications, for example during the conventional spark discharge. The plasma generated in these applications is usually called "thermal plasma". In the kinetic enhancement, high-energy electrons and ions are produced, particularly active radicals (O, OH, H, etc.) by means of electron impact dissociation, ion impact, recombination dissociation and collisional dissociation of reactants with excited molecules. Moreover, plasma can produce long-lifetime reactive species, e.g. ozone O_3, or catalytic intermediate species, e.g. NO, which can further speed up low-temperature fuel oxidation. Overall, in the RF corona ignition systems, the kinetic and thermal effects are known to be predominant. These aspects can produce a considerable increase in the early flame growth speed, consequently reducing ignition delay timings, making the kernel formation less susceptible to fluctuations, and therefore extending lean stable operating limits of the engine.

The effectiveness of corona systems in extending the ignition lean stable limits and reducing ignition delay time was tested in a pressurized vessel with gaseous fuels by Wang et al. [50]. Yu et al. [51] evaluated the ability to ignite premixed mixtures under both quiescent and turbulent conditions in an optically accessible constant volume chamber using methane-air and propane-air mixtures ranging from stoichiometric conditions to the lean ignitability limits. They found that the corona is able to initiate multiple ignition spots in proximity of the igniter and continuously impact the ignition flame propagation when a long energizing period is employed. They also tested RF corona igniters under real engine operating conditions. In the work of Pineda et al. [52], the EGR tolerance increase with respect to a conventional spark was found to be of 10-15% at boosted operation and 16-25% at naturally aspirated operation. Schenk et al. [53] compared the corona to a transistor coil ignition system showing the advantages of the corona system at high engine load, especially in the context of high in-cylinder charge motion. Bresler et al. [54] made a comparison among a conventional spark igniter and other solutions (3-plug, multi-strike, continuous discharge, plasma, and corona discharge ignitions) for a GDI turbocharged engine. They found improvements in terms of fuel consumption, CCV, and EGR tolerance by using corona systems. Corona ignition was also studied in optical engines. Idicheria and Najt [55] performed flame morphological analysis without quantitative image-based results in a gasoline-fueled engine and found that corona ignition system allows for more robust ignition, flame kernel formation, and flame propagation by producing multiple ignition sites compared to the single spark location. In the work by Marko et al. [56] on natural gas engines, in addition to the morphological analysis of the flames, quantitative results of projected flame area based on imaging analysis are reported, at a single combustion stage, comparing RF corona and spark. Cimarello et al. [57, 58] compared RF corona and conventional spark on an optical access engine, and a sensitivity analysis of the main corona control parameters was carried out. Cruccolini et al. [59] tested an RF corona discharge igniter in an optical engine fueled with methane and hydrogen-methane blend and a lean limit extension was found for both fuels. Flame speed increase during combustion onset was assessed through indicating measurements and high-speed image acquisitions.

To characterize the thermal and kinetic features of the discharge, non-equilibrium plasma streamers have been investigated in recent years by using both experiments and simulations. The main goal of these studies was to characterize their effect on ignition and to quantify the amount of radicals and excited species generated by the electrical discharge. Mostly canonical electrode geometries (point-to-plane, pin-to plane, pin-to-pin) with simple excitation schemes (constant or pulsed voltage) were investigated. Eichwald et al. [60] modeled a positive corona discharge in air for a point-to-plane geometry. They found that monoatomic oxygen is mainly produced in the secondary streamer, in agreement with experiments carried out with TALIF diagnostics. Qin and Pasko [61] found that the streamer development (growth, decay, stable propagation) is affected not only by the external field, but

the dimensions of the streamers also play an important role. Bagheri et al. [62] compared six different numerical codes to model positive streamer discharges, considering three benchmark cases: they demonstrated that a good agreement between models can be found when fine grids and small time-steps are used. Breden et al. [45] modeled the discharge obtained with a corona igniter and a dielectric barrier discharge igniter. They found that the dielectric barrier self-limits the discharge, avoiding the streamer-to-arc transition, but also resulting in a total radical yield that saturates in time. On the contrary, the radical yield of the corona can continuously increase in time. Scarcelli et al. [63, 64] and Zhang et al. [65] modeled a nanosecond pulsed discharge generated by a real pin igniter geometry. The comparison with experimental results showed good agreement regarding bulk gas temperature and atomic oxygen concentration. Also, the streamer-to-arc transition regime was accurately reproduced. The same nanosecond pulsed discharge igniter was tested by Wolk and Ekoto [66] which performed pressure-rise calorimetry and direct imaging of atomic oxygen and molecular nitrogen emission, evaluating radical production and streamer-to-arc transition. As for RF corona ignition, Cruccolini et al. [67] performed the first plasma modeling of a corona discharge with realistic igniter geometry and sinusoidal excitation cycles at 1 MHz. They found that atomic oxygen is generated in axial direction during the discharges, before spreading away due to shock waves. The cumulated atomic oxygen production is found to increase monotonically with time, cycle after cycle, and its rising behavior can be approximated by a linear function.

From this extended review on the thermo-physical processes related to the corona ignition, a lack of modeling work on real engine applications clearly arises. CFD simulations have the potential to enlighten crucial aspects and parameters that determine engine behaviors with corona ignition. To the best of authors' knowledge, no CFD studies are available in the literature concerning the simulation of a full internal combustion engine ignited by corona discharges. Within the context of plasma-assisted ignition systems utilized in ICEs, numerical simulations of an actual combustion process can be very informative, therefore, this forms the main objective of this work, so far lacking in the scientific literature.

Simulations can assist in understanding the interaction between the igniter and the flow field and in studying the combustion behavior in lean mixture conditions. After an initial study simply under stoichiometric conditions reported in [68], the aim of the present work is to numerically investigate the engine behavior with corona ignition at various air-fuel ratios (ARF), up to unstable points, and compare the findings against the traditional spark ignition. The ignition model is based on energy and active radical depositions. First the effects of the deposition region shape and dimensions and the amount of deposited atomic oxygen are investigated, to assess the robustness of the model and understand the main controlling parameters. Simulation predictions are then validated against optical engine experiments, in terms of fuel mass burned and flame imaging. The results show that the engine lean limit can be predicted though RANS simulations looking at the duration of the initial kernel development. The corona discharge extends the stable operation by about 0.2 lambda points, with respect to a spark ignition, and the simulations contribute to elucidating the mechanisms producing these results.

OPTICAL ACCESS SI ENGINE DESCRIPTION

Experimental data have been presented and discussed extensively in [57, 58], and only a brief description of the available data is reported here, for the sake of comprehensiveness. The optical engine, shown in Figure 1, is a 500 cm^3 single cylinder engine with pent-roof combustion chamber, four valves and reverse tumble intake port design, that can be operated in Port Fuel Injection (PFI) or Direct Injection (DI) mode. In this study PFI is used, with standard market European gasoline fuel [69, 70]. The combustion chamber is optically accessible through a 60-mm diameter quartz window in the piston crown [71]. A Bowditch-type prolonged piston is used to accommodate a 45-degree mirror which allows the optical access from the bottom. Graphite rings are used to avoid lubricant presence in the combustion chamber, maintaining the quartz window clean.

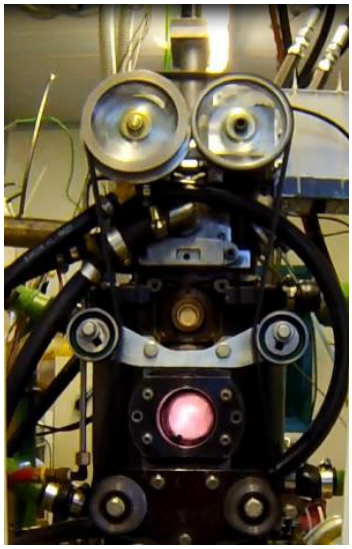

Figure 1. Optical access engine in firing condition.

The engine was controlled in terms of speed, throttle position, AFR, injection and ignition timing. Speed control was obtained by means of an AVL 5700 dynamic brake, which is coupled to the optical engine. The air flow was set by maintaining the throttle valve at a fixed position for the entire experimental campaign, ensuring a constant airflow and tumble motion. A dedicated ECU was used to regulate the AFR by controlling the gasoline injected mass and to command the ignition start. This control strategy results in a decreasing engine load as the AFR is increased. A piezoresistive transducer (Kistler 4075A5) installed on the intake port measures the intake pressure and a piezoelectric transducer (Kistler 6061 B) installed on one side of the chamber measures the in-cylinder pressure. The angular position of the crankshaft is measured by an optical encoder (AVL 365C) with 0.1 CAD resolution. In each operating point, 100 consecutive cycles are recorded and post-processed. A Vision Research Phantom V710 high-speed CMOS camera coupled with a Nikon 55 mm f/2.8 lens was used to obtain flame images recording the natural luminosity. The sampling rate was 20 kHz, corresponding to 0.3 CAD/frame at 1000 rpm, and with a spatial resolution of 0.123 mm/pixel. Images are recorded in sync with the indicated pressure, collecting 63 consecutive combustion events for each operating condition. The main engine features are given in Table 1. The ignition timing is adjusted to the Maximum Brake Torque (MBT) value as shown in Table 2, for each mixture condition, and for each igniter.

Table 1. Engine data and operating conditions.

Displacement	500 cm^3
Bore	0.085 m
Stroke	0.088 m
Connecting rod	0.139 m
Compression ratio	8.8:1
Number of valves	4
Engine speed	1000 rpm
Indicated Mean Effective Pressure	~5 bar @ λ=1
Intake valve open	329 CAD aTDC
Intake valve close	547 CAD aTDC
Exhaust valve open	170 CAD aTDC
Exhaust valve close	380 CAD aTDC
Fuel	Standard European Gasoline, RON 95 MON 85
Injection	PFI

Table 2. Experimental ignition timings.

λ [–]	Spark Ignition Timing [CAD bTDC]	RF Corona Ignition Timing [CAD bTDC]
1.0	20.5	6
1.2	25	9
1.4	40	16
1.5	46.5	-
1.6	-	32
1.65	-	32.5
1.7	-	35

COMPUTATIONAL METHOD

In this work, the CONVERGE v3.0 CFD software package [72, 73] is used as the computational framework for the simulations. Figure 2.a shows the computational domain, divided in five different regions, i.e., plenum, throttle body, intake port, combustion chamber and exhaust port. Since the engine is operated at part load, the throttle in its actual position is included in the 3D domain. The code allows the calculation of the three-dimensional, compressible, chemically-reacting flows in complex geometries with moving boundaries, and it is specifically tailored for piston engine analysis. The code uses a modified cut-cell Cartesian method that eliminates the need for the computational grid to be morphed into the geometry of interest, while still precisely representing the actual boundary shape. This approach allows for the use of simple and efficient orthogonal grids, and completely automates the mesh generation process. (Figure 2.b).

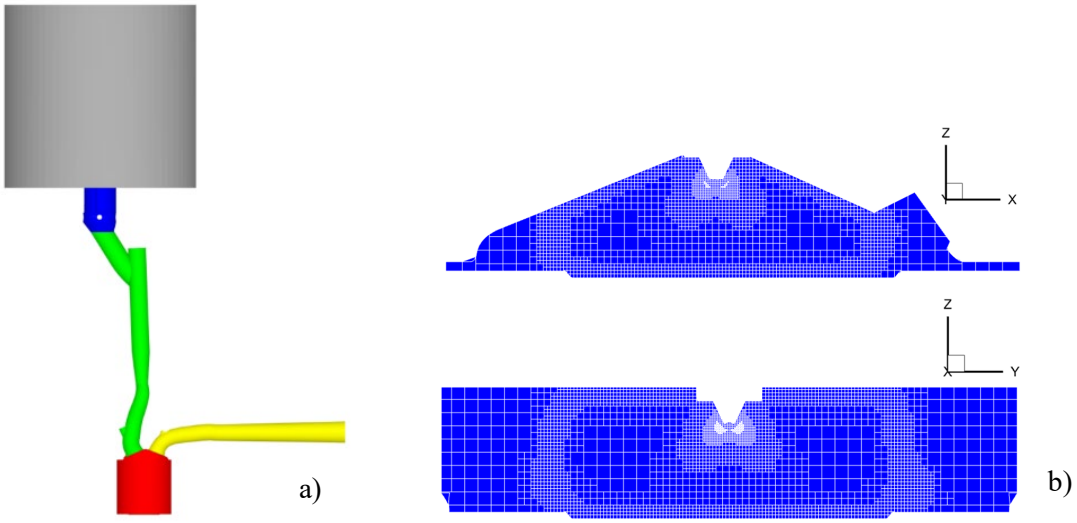

Figure 2. CFD engine model. Geometry: plenum in grey, throttle body in blue, intake port in green, combustion chamber in red and exhaust port in yellow (a). Mesh (b).

The finite volume method is used to solve the overall set of compressible Favre-averaged equations. Conservation of mass and momentum are solved via a pressure-velocity coupling algorithm, using the Pressure Implicit with Splitting of Operators (PISO) method [74]. The transport equations of energy and species are solved after the momentum predictor and the first corrector have been completed. Turbulence is solved after the PISO loop is converged. Spatial discretization is second-order and time integration is based on the first order Euler implicit

scheme, with variable timestep controlled by convective CFL below 1 during the combustion phase and 1.5 elsewhere.

The modeling approach is based on the RANS equations, using the Standard k-ε turbulence model. The PSR combustion model is adopted without turbulence-chemistry interaction. The SAGE chemical solver calculates the reaction rates for each elementary reaction within each cell, while the CFD solver takes care of the transport equations. Gasoline chemical kinetics has been modeled using the reduced mechanism based on the work of Liu et al. [75] for the primary reference fuels (PRF) iso-octane and n-heptane, consisting of 48 species and 152 reactions. To model this blend, 95% of iso-octane and 5% of n-heptane by volume is used. Fuel injection is not modeled directly, but fuel and air are perfectly mixed at the inlet boundary. Boundary conditions have been derived from experiments and basically consist of time-varying values of static pressure and temperature for the inflow, and static pressure for the outflow. In each engine point, multiple cycles were simulated to remove unwanted effects due to the initialization. Generally, it was observed that from the third cycle RANS results became repeatable, therefore, all the analyses presented in this work were done on the last simulated cycle.

Combustion is initiated by a mix of energy and species deposition, without attempting to model the complex phenomena underlying ignition, especially because for alternative igniters no established literature is available. Depositions are characterized by a uniform spatial and temporal distribution. For the spark case, the deposition is on a sphere between the electrode and counter-electrode (Figure 3.a): 2.5 mJ for 0.5 CAD, to simulate the breakdown/arc phase, and additional 2.5 mJ for 10 CAD, to simulate the glow phase, are released into the gas as indicated by measurements reported in [76] for this specific spark plug and conditions. For the RF corona case, the source region is represented by four long and narrow cylinders (Figure 3.b): the deposition duration is 1.8 CAD, equivalent to commanded discharge duration of 300 μs at 1000 rpm. As it will be discussed later, cylinder length and diameter are among the investigated parameters. The deposited energy varies according to the engine conditions between 120 mJ (at stoichiometric condition) and 35 mJ (at the leanest mixture condition) as specified by the available corresponding experimental values [77]. Simultaneously, an amount of atomic oxygen, identified through parametric exploration around literature data [60 - 67], is also added, since atomic oxygen is the primary active radical produced by an RF corona discharge in air [60]. In particular, Cruccolini et al. [67] studied the same RF corona discharge used in this work modeling the axisymmetric and transient process of non-equilibrium plasma generation. They found a range of atomic oxygen production between $2.5 \cdot 10^{-9}$ and $8.5 \cdot 10^{-9}$ kg per discharge event of 300 μs on 4 pins. This data range is central to modeling the combustion process initiated by the non-equilibrium plasma investigated in this paper. It is also worth pointing out that the deposition of just atomic oxygen, despite might appear simplistic, is supported by several studies like [60] because other radicals such as OH are then produced from O. It would also be almost impossible to include a detailed plasma chemistry together with the fuel combustion kinetics, as of today.

Spark and corona ignition timings were set as in the engine experiments (cf. Table 2). Figure 4 shows an example of the temperature plot for the spark (Figure 4.a) and corona igniter (Figure 4.b) at stoichiometric conditions, 1 CAD after the ignition timing. The slicing plane is different to accommodate the main features of the ignition source, i.e., ZX plane through the ground electrode for the spark case, a plane rotated by 45 degrees slicing through two tips and streamers for the corona igniter.

Various fixed and adaptive meshing refinement (AMR) strategies are used, ad-hoc temporally and spatially activated. Fixed mesh refinement is used in the cylinder, in the valve seat regions and in the source regions. Temperature-based AMR is used to resolve the flame front during the combustion, and velocity-based AMR is used elsewhere to resolve complex flow structures. More details on the grids used are provided in the Table 3. A

mesh sensitivity study has already been done for similar applications [70], and this mesh setup follows the common best practices for engine RANS simulations using a grid size of 0.125 mm around the igniter (Figure 4.c.d).

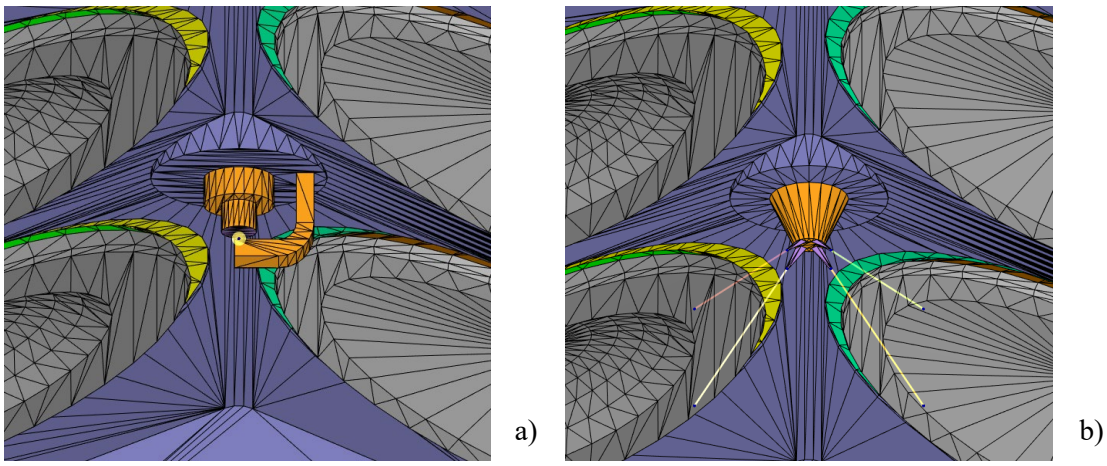

Figure 3. Deposition regions. Spark (a). Corona (b).

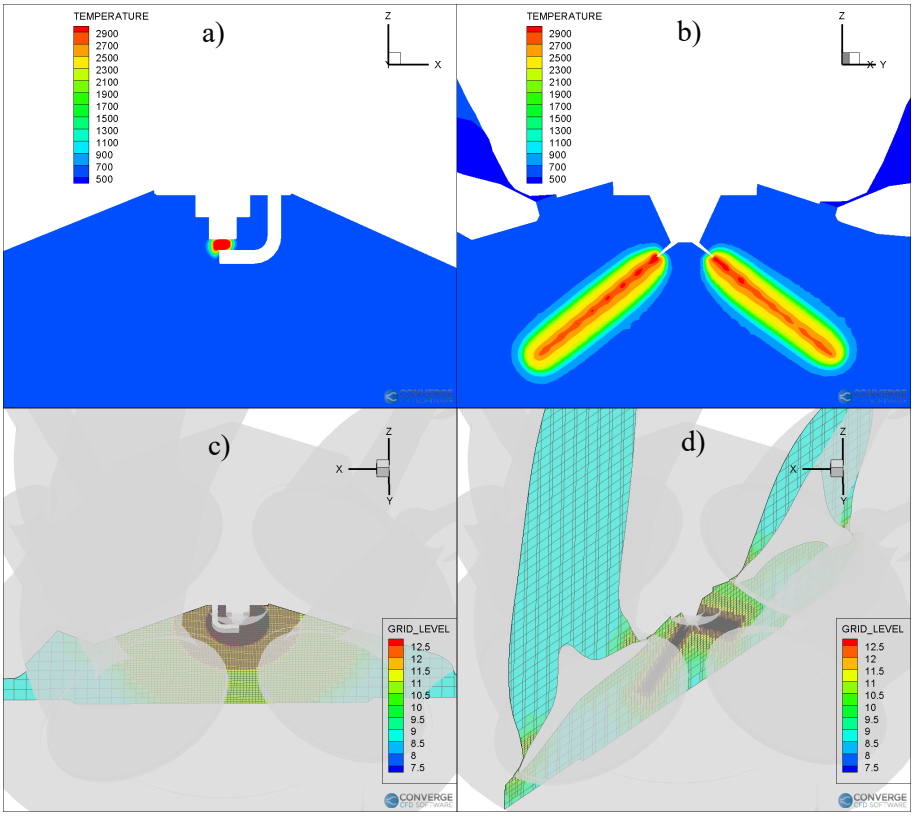

Figure 4. Temperature contours and grid resolution for spark and corona igniters at λ=1, visualized 1 CAD after the ignition timing.

Table 3. Mesh details.

Maximum grid size in the cylinder and ports	2 mm
Velocity AMR size	1 mm
Temperature AMR size	0.5 mm
Minimum grid size (around igniter)	0.125 mm

Maximum number of cells	1 500 000
Restitution time (hours/cycle)	40

RESULTS AND DISCUSSION

Results presentation and discussion are organized as follows. First, the simulation results for the conventional spark igniter at different AFRs are presented, as baseline model assessment. Then, the corona igniter is studied in depth, analyzing the effect of the length and the diameter of deposition region, and the amount of deposited atomic oxygen. Finally, an overview of the flame development is presented, focusing on the first stages of the combustion.

The combustion analyses are quantitatively conducted in terms of normalized cumulative heat release and corresponding mass fraction burned (MFB). Pressure traces are not directly comparable because the optical engine data is affected by non-negligible blow-by, while the CFD model does not attempt to account for these effects due to their complexities which would be outside the scope of this work. Flame structure is also qualitatively analyzed by comparing experimental flame images with volume renderings of the computed temperature fields.

Combustion initiated by spark ignition

Spark discharge is an unsteady process that consumes a large amount of energy and has less kinetic enhancement effect in combustion compared to non-equilibrium plasmas [47, 25, 36]. Here, the effect of atomic oxygen deposition for a spark discharge is investigated. Figure 5 shows the comparison between experimental and numerical results for the combustion started by a spark, at $\lambda = 1.0$. The black curve is the average experimental MFB, the red curve is the corresponding numerical simulation obtained by using energy deposition as ignition source, while the dotted blue curve is the combustion initiated with combined energy and radical deposition. The radical deposition consists of $5 \cdot 10^{-9}$ kg of atomic oxygen, O, with a corresponding amount of molecular oxygen, O_2, removed, to balance overall mass; the effect of this value will be justified and discussed in more detail later in the next paragraph. The experimental combustion rate is very well reproduced by the simulations. Numerical combustion rates with and without radicals are perfectly overlapped indicating that, as expected, the presence of atomic oxygen is irrelevant in standard spark ignition at stoichiometric conditions. The effect of the presence of atomic oxygen has also been investigated for cases with different AFR values, confirming that the radical deposition does not produce differences in the burning rate. To better understand this phenomenon, a comparison of the predicted maximum local temperature in the spark region during the ignition phase is shown in Figure 6. Even if the presence of radicals increases the peak local temperature, the levels involved already exceed 10,000 K, therefore, the thermal effect dominates [47]. The bulk gas temperature achieved with the conventional spark discharge is far above the low-temperature plasma range where radicals can have an impact in enhancing the combustion.

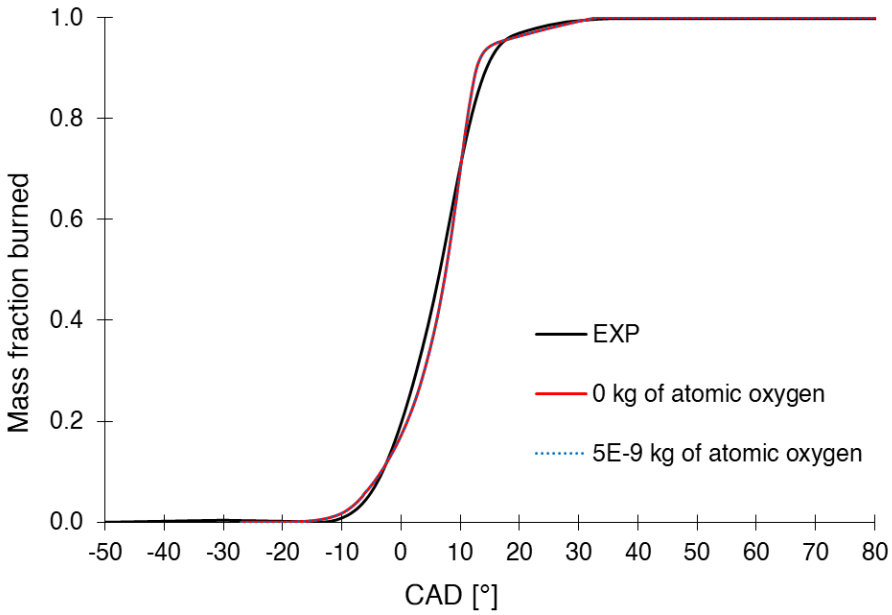

Figure 5. Comparison of MFB for stoichiometric combustion with spark ignition.

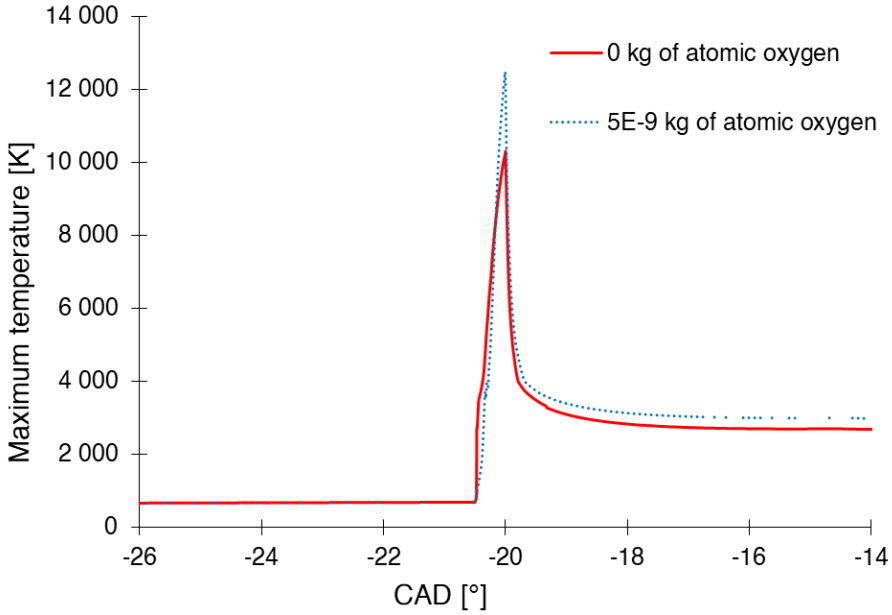

Figure 6. Effect of atomic oxygen deposition on maximum local temperature during the ignition stage, with spark igniter at λ = 1.0.

In addition to the stoichiometric condition, two additional lean conditions have been tested for the spark ignition, i.e., λ = 1.4 and λ = 1.5. Figure 7 shows all three experimental MFB curves and the corresponding numerical results. The ignition timing for each simulation case is set to the experimental value (Table 2) and no atomic oxygen deposition is considered. The results clearly show that the combustion rate for the stoichiometric case is faster than the corresponding rates for the lean cases. Since the behavior under different λ values is well reproduced by the combustion simulations ignited solely with thermal energy deposition, it can be inferred that the spark ignition process is driven by the initial high-temperature thermal plasma (see Figure 6 again) and the impact of atomic oxygen is irrelevant.

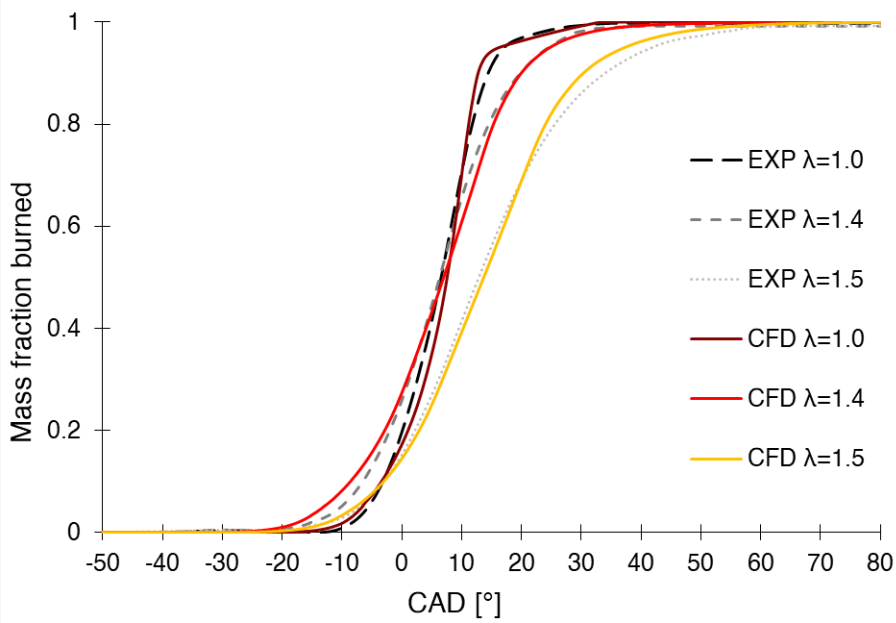

Figure 7. AFR effect on MFB (λ = 1.0, λ = 1.4 and λ = 1.5) with spark ignition: experimental average cycle (dashed lines), numerical RANS cycle (solid lines). Only thermal energy is deposited, no atomic oxygen.

Combustion initiated by corona ignition

The corona ignition concept is different and its ignition process is expected to be sensitive to both energy and atomic oxygen depositions. As it will be shown in the following, active radicals play a role in the combustion initiation. In addition, the length and shape of the streamer plasma channel are key features of the corona ignition system, which require specific care.

Results of the experimental imaging tests reported in Table 4 show that the corona driving voltage and discharge duration affect the streamer size, number and branching [58]. The driving voltage is a control parameter that affects the peak electrode voltage, having a strong impact on discharge and combustion behavior, as investigated by Cimarello et al. [58] and Discepoli et al. [77]. The streamer structures are visualized in Table 4 at different relative air-fuel ratios, 1 CAD after the ignition command. The observation reveals that the streamer length decreases as λ increases. The averaged streamer features are reported in the same table under each image, i.e. streamer length, ignition timing, driving voltage, charge density and thermal energy deposited on the gas. It is worth noticing that the natural luminosity detected by the camera reduces increasing λ, and images are not normalized for this effect. Despite this observation, it is quite evident that the four streamers shorten at larger λ values. However, some uncertainty on the exact length data persists. During the engine tests, the ignition timing is adjusted to the MBT for each mixture condition, i.e., the start needs to be advanced to accommodate the longer combustion duration under lean conditions. The value of the driving voltage is the maximum possible level that guarantees a stable corona discharge and avoids arc formation. The deposited energy values under engine conditions are derived from the available corresponding experimental dataset [77] collected in a constant volume chamber, interpolating for the actual pressure, temperature and voltage. The estimated atomic oxygen deposition is calculated from results of Cruccolini et al. [67] that performed the first plasma modeling of a corona discharge with realistic igniter geometry and sinusoidal excitation cycles at 1 MHz. Case 3 of [67] corresponds to the engine conditions explored in this work in terms of gas density at the ignition timing. For that case, a single streamer discharge produces 3.9 mg/s of atomic oxygen. Since the discharge duration is $300 \cdot 10^{-6}$ s, the atomic oxygen deposited mass is calculated as 3.9 mg/s · $300 \cdot 10^{-6}$ s = $1.17 \cdot 10^{-3}$ mg. This value has been multiplied by 4, since 4 streamers are produced for each discharge: $1.17 \cdot 10^{-3}$ mg · 4 = $4.7 \cdot 10^{-3}$ mg ≈ $5 \cdot 10^{-9}$ kg.

Table 4. Structure of the corona streamers 1 CAD after ignition and average streamer data for different mixture conditions. Bold data are directly used in the CFD models.

λ	1.0	1.2	1.4	1.6	1.65	1.7
	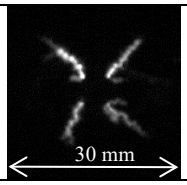	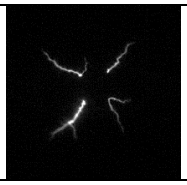	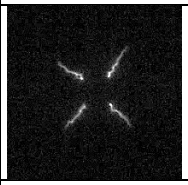	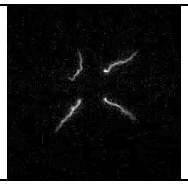		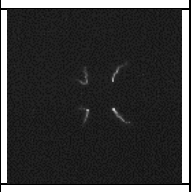
Streamer length [mm] [77]	**10**	**9.5**	**6.5**	**7**	**7.5**	**6**
Ignition timing [CAD bTDC] [77]	**6**	**9**	**16**	**32**	**32.5**	**35**
Driving voltage [V] [77]	53	49	40	34	34	30
Gas density [kg/m^3] [77]	6.25	6.05	5.40	3.70	3.65	3.45
Measured thermal energy deposited on the gas [mJ] [77], over 300 µs	**120**	**100**	**55**	**45**	**40**	**35**
Estimated mass of atomic oxygen [kg] [67], generated over 300 µs	**$5\cdot10^{-9}$**	**$5\cdot10^{-9}$**	**$5\cdot10^{-9}$**	**$5\cdot10^{-9}$**	**$5\cdot10^{-9}$**	**$5\cdot10^{-9}$**

Based on the above observations, in the CFD simulations streamers are modeled assuming that energy and radicals can be deposited on four long and narrow cylindrical regions (Figure 3.b, and Figure 4.b,d). Since it has been observed that the geometrical feature assumptions have a substantial impact on the simulation results, the effect of length and diameter of these cylinders on the combustion development has been explored and reported here. Figure 8 shows the results of this investigation in stoichiometric conditions, where the length suggested by the experimental imaging is 10 mm. The experimental MFB (black curve) is compared with numerical curves obtained with perturbed lengths (10 mm, 7.5 mm and 5 mm) and different diameters (0.125 mm and 0.25 mm). An additional limiting case is included, resembling the spark deposition approach with four spherical regions (yellow curve) having the same volume of the cylinders. Combustion rate obtained with the 10 mm length reproduces very well the experimental trend at $\lambda = 1.0$. Using shorter cylinder lengths, the start of combustion is delayed while the main part of the turbulent combustion development is unchanged. On the contrary, the diameter does not produce appreciable effects on the combustion rate, within the range of values tested and also considering the minimum grid resolution adopted.

A further investigation is carried out to better understand the interaction between the streamer geometry assumptions and the subsequent combustion development. The maximum local temperature during the ignition process, shown in Figure 9, increases for smaller cylinder volumes. For the case with spheres, it goes even farther, well above 10,000 K, despite the spheres volume is the same as the 10x0.25 mm cylinders case. The area-to-volume ratio has a major impact on local temperatures. Despite this, combustion rates present a completely opposite trend: combustion develops faster using longer cylinders where the initial temperature remains lower, while using spheres that generate high temperatures combustion develops more slowly. The explanation of this behavior can be provided by observing the temperature contours in Figure 10. These images show the simulated

flame propagation around the corona streamers location, at three instants after the ignition on a cut plane passing through the kernels. Differences in the flame propagation over time reflect differences in the global combustion progress. In particular, the flame shape strongly varies in terms of surface area. The simulation with high area-to-volume ratio of the initial kernel is characterized by a larger burnt gas zone and a wider flame at the same time instants, whereas the simulation with spheres, i.e. with the lower area-to-volume ratio, shows a retarded flame region. The flame expansion highlights that, using longer cylinders, flame is able to propagate from the very beginning, and grows much faster towards the rest of the chamber. On the other hand, using more compact cylinders or spheres, kernel propagations are progressively hindered, and flames are confined near the igniter for longer times. In essence, as long as the local temperature reaches values above about 3000 K, the overall flame propagation is mainly affected by the flame area, and therefore by the mass and heat diffusion processes, rather than by the chemical reactivity which remains very high.

A similar behavior has also been observed for lean mixture cases, but not reported for the sake of brevity. Overall, this suggests that the streamer penetration, generated by the corona discharge, plays a critical role in the kernel development, their initial length being the main influential parameter affecting the engine combustion performance.

Having assessed the effects of the ignition source geometrical aspects, it can then be observed that the best match in Figure 8 is obtained by utilizing the actual measured length, i.e., l=10 mm. Therefore, for each mixture condition that will be investigated in the rest of the of this work, streamer lengths derived from experimental imaging will be assumed as the most reliable (Table 4). Regarding the diameter, being results rather insensitive to the values tested, a constant value of 0.25 mm will also be kept, in order to have a larger number of computational cells falling inside the deposition regions.

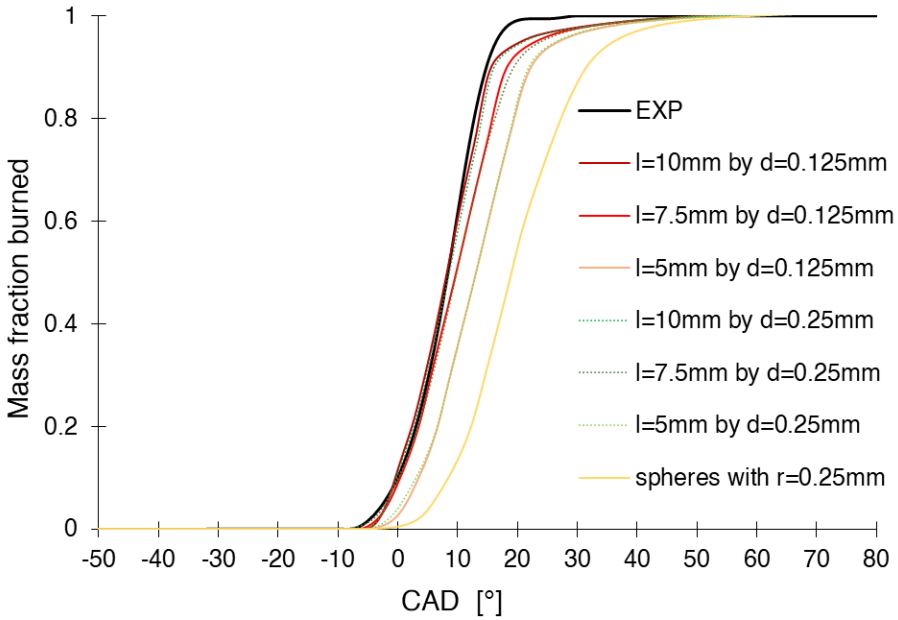

Figure 8. Effect of cylinders length on MFB in stoichiometric conditions.

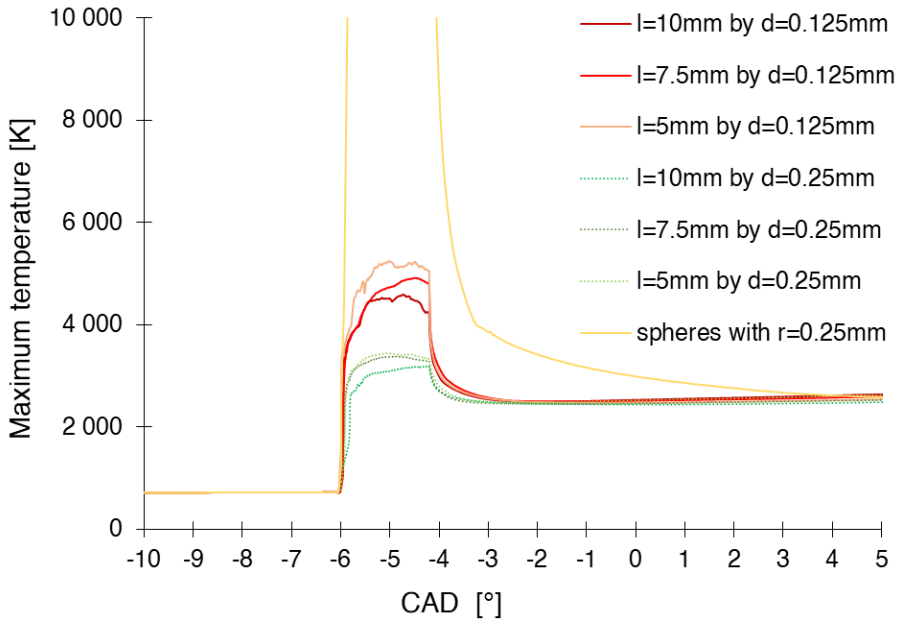

Figure 9. Effect of cylinders length on maximum temperature during the ignition stage, in stoichiometric conditions.

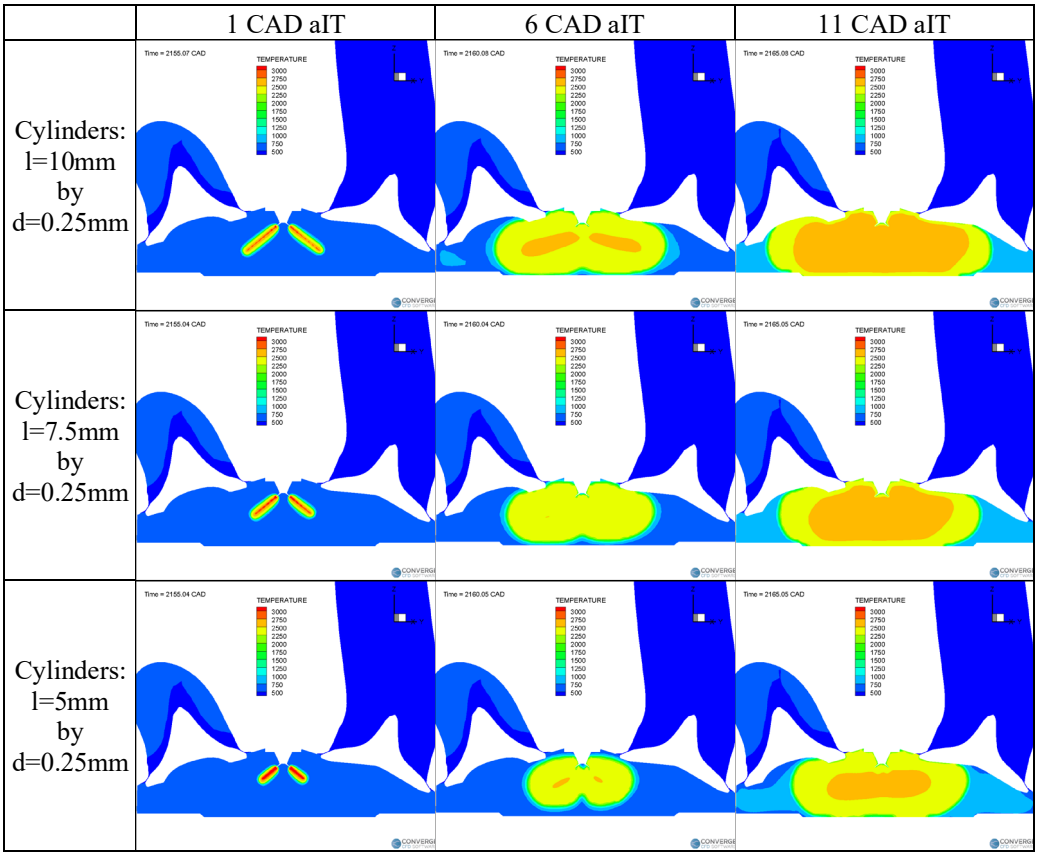

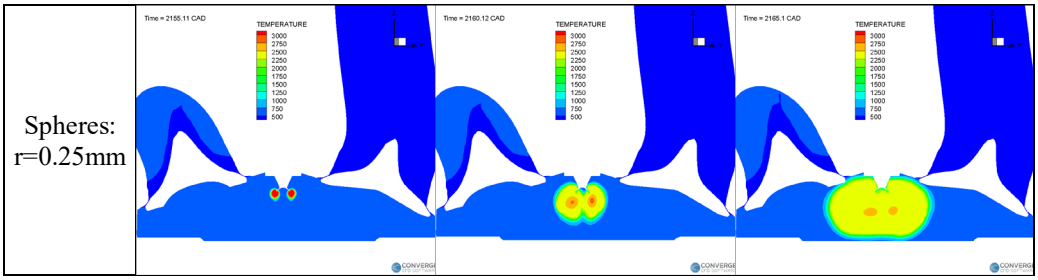

Figure 10. Temperature fields (range 500-3,000 K), at 1, 6, and 11 CAD after ignition timing, in stoichiometric conditions.

As discussed in the introduction, the main objective of the work is the quantification of the role of non-equilibrium plasma with low-temperature active radicals. Therefore, the focus of the analysis will now switch to understanding the impact of the atomic oxygen on kernel growth and combustion rates originated from corona discharges.

Predictions of the engine combustion process are shown in Figure 11 at $\lambda = 1.0$ (a) and $\lambda = 1.6$ (b), against corresponding measurements. The black dashed curve is the experimental average cycle for each case. Colored curve bundles provide the sensitivity to the amount of radicals deposited in the form of atomic oxygen, with varying shades of green and blue, at $\lambda = 1.0$ and $\lambda = 1.6$, respectively. The explored values range from absolute no radicals up to a very large amount of $1 \cdot 10^{-8}$ kg of O, if compared to the expected values [67] reported in Table 4. The deposition of atomic oxygen requires a mass compensation, as previously mentioned, since atomic oxygen is chemically created by decomposition from O_2. A lack of compensation would lead to local alterations of the mixture conditions, with unphysical results at increasing concentrations. Focusing, for instance, on stoichiometric conditions (Figure 11.a) the atomic oxygen is shown to have a double effect, one on the ignition delay and one on the subsequent flame speed.

1. The first one is visible in the early combustion stage, since atomic oxygen reduces the kernel development time confirming that radicals are ignition promoters. In addition, the early flame growth is also accelerated (up to CA10). As a matter of fact, from a fundamental point of view, the effect of atomic oxygen addition is expected to increase the laminar flame speed, as shown in Appendix (Figure A 1), by about 10% to 15%, in the current operating conditions of the corona discharge igniter.
2. The second one refers to the main turbulent combustion development (CA10 to CA90), which is characterized by a marginally faster flame growth speed, as observed by the curve slopes at varying deposited oxygen mass. The justification can be the late combustion phasing achieved with less amount of oxygen radical, leading to slightly lower temperatures in the chamber and therefore lower flame speed.

At $\lambda = 1.0$ the model, considering the expected amount of atomic oxygen $5 \cdot 10^{-9}$ kg [67], matches the corona experimental combustion progress, suggesting that the adopted initial value is close to reality.

The impact of O presence in the plasma channel is amplified when the mixture is lean, as visible at $\lambda = 1.6$ (Figure 11.b). The two effects mentioned above are well visible also in lean operation. In this case the model, despite underpredicting the measured turbulent combustion rates (CA10 to CA90), is accurate enough in estimating ignition delays and kernel growth durations (up to CA10) if the best estimate for the amount of O is used, i.e., $5 \cdot 10^{-9}$ kg (Table 4). It is also very important to note that with lower or no amount of radicals misfires are predicted.

A comparison of the maximum local temperature obtained from the simulations during the ignition phase is shown in Figure 12. The atomic oxygen deposition increases the maximum local temperature during this phase. The impact of radicals is now substantial, as opposed to what was observed for the spark case (Figure 5 and Figure 6). In the corona ignition process the combustion rate changes in response to a variation in the initial O concentration. Since the maximum temperature reached in the ignition stage is now much smaller than in the spark case, and the regime is much closer to a non-equilibrium low-temperature plasma, the chemical kinetic enhancement due to the active species become very relevant.

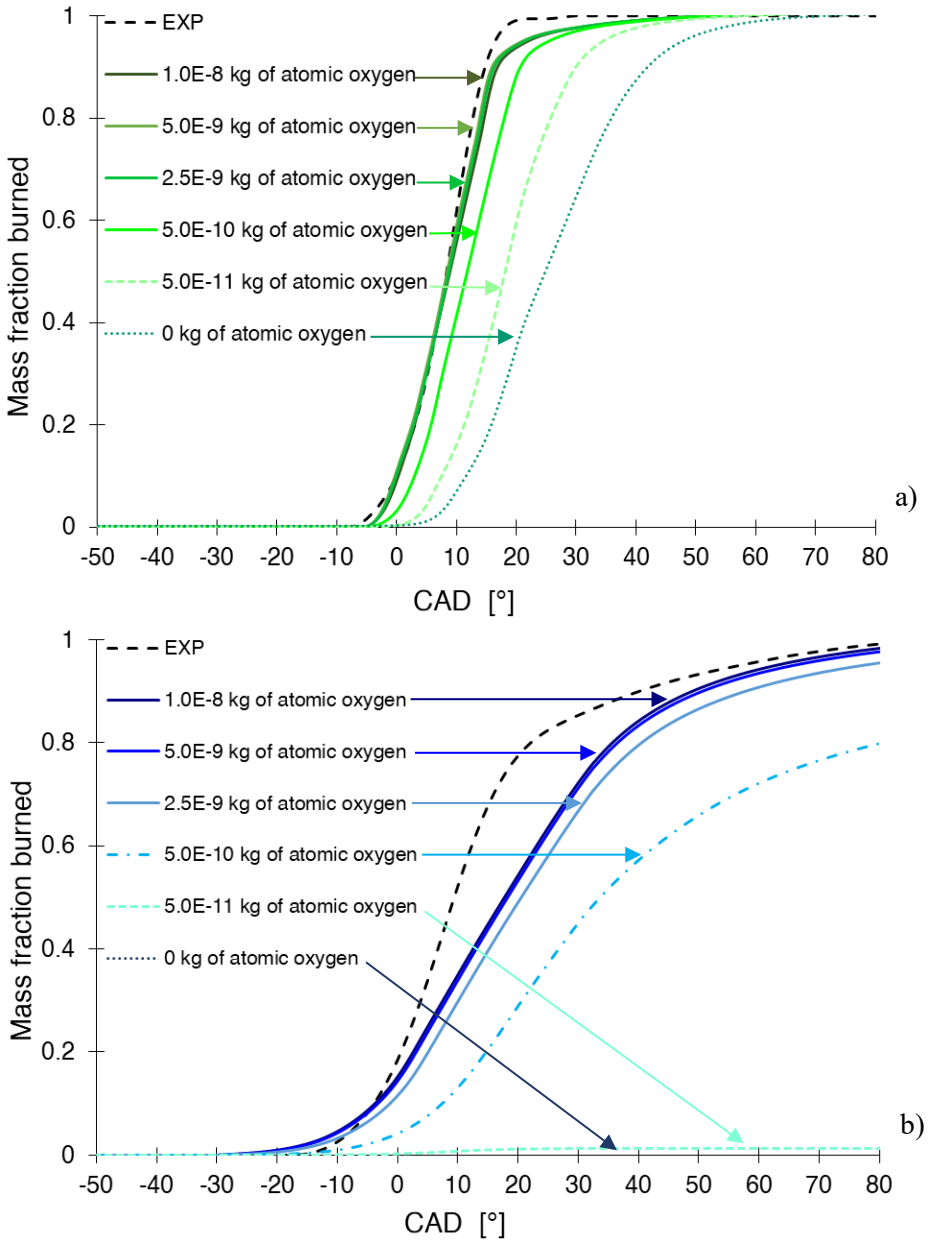

Figure 11. Effect of atomic oxygen deposition on MFB, at λ = 1.0 (a) and λ = 1.6 (b).

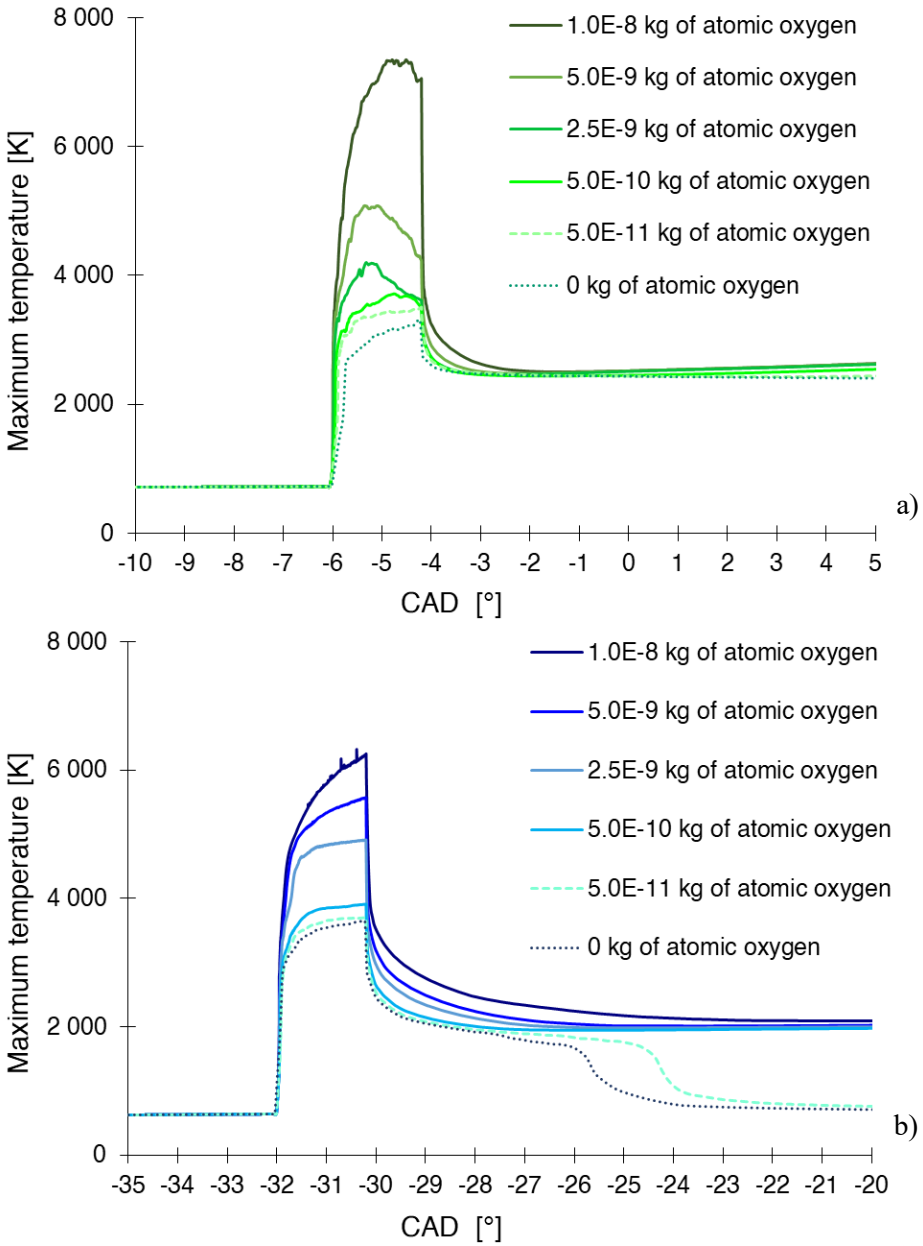

Figure 12. Effect of atomic oxygen deposition on maximum local temperature during the ignition stage, at λ = 1.0 (a) and λ = 1.6 (b).

Beside the stoichiometric condition, three additional mixture conditions have been simulated for the corona ignition, i.e., λ = 1.4, 1.6 and 1.7. The ignition parameters are again specified according to the available measurements in each case, in order to reproduce the experimental conditions and values. Table 4 lists these values used for the CFD model setup. The amount of deposited atomic oxygen is kept fixed, at the level of $5 \cdot 10^{-9}$ kg, according to the best available estimate from the work of Cruccolini et al. [67]. It is also worth noticing that as λ increases streamer lengths and deposited thermal energies are decreased.

Figure 13 shows the predicted MFB curves compared to the experimental measurements. As expected, as the mixture gets leaner the combustion progress decelerates, and remarkably, simulations are able to capture this trend. The predicted combustion rates, however, seem to have a shorter flame kernel development compared to the experiments, as the kernel growth transitions to flame propagation earlier and the turbulent burning rate is slightly slower in the simulations, except for λ = 1.0 where the agreement is adequate. This underestimation of the

combustion rate is particularly evident for λ = 1.6 case, while for the leanest case (λ = 1.7) the gap between numerical and experimental results is reduced. Overall, the results in Figure 13 support the fact that RANS calculations are able to predict combustions initiated by corona discharge ignition systems, provided the spatial description of the ignition source and the presence of active radicals are properly evaluated.

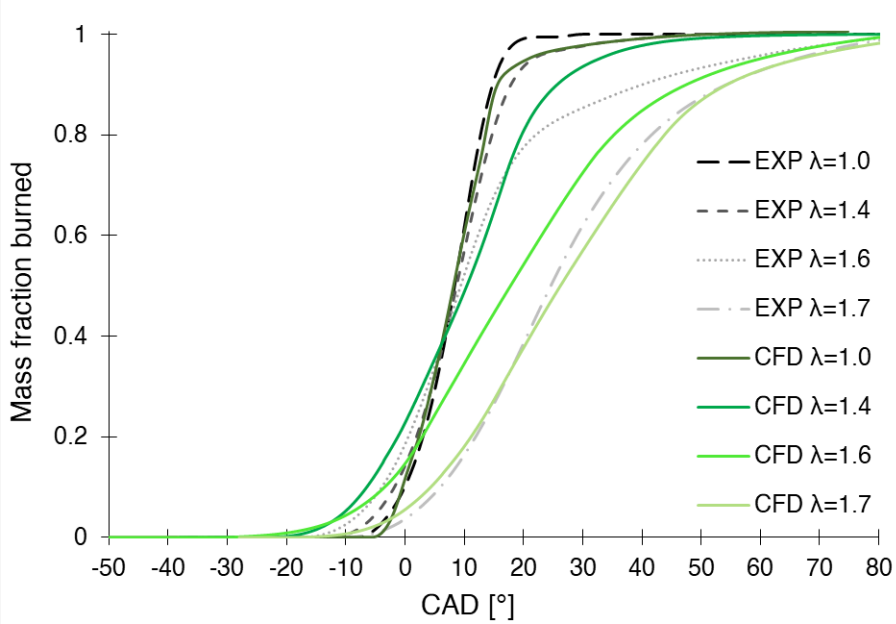

Figure 13. AFR effect on MFB (λ = 1.0, λ = 1.4, λ = 1.6 and λ = 1.7) with corona igniter: experimental average cycle (dashed lines), numerical RANS cycle (solid lines). Ignition parameters as in Table 4.

Comparison between spark and corona ignition – Combustion analysis

After the extensive parametric model assessment and validation presented above, the combustion started by the two different igniters is now compared. Figure 14 shows the two MFB curves at λ = 1.0 reported from the ignition timing. The spark timing is 20 CAD bTDC, while the corona ignition timing is 6 CAD bTDC (as listed also in Table 2). The advantage of the corona ignition compared to the conventional spark discharge mainly concerns the beginning of the combustion up to about CA10, as clearly observed also in [57 - 59]. The corona discharge shortens the kernel formation stage by about 10-12 CAD. The simulations reproduce this aspect correctly. The turbulent combustion rate is then quite similar, in that after the kernel growth stage the turbulent flame front propagation is not influenced by the igniter anymore, being the flame far away from it. This aspect will be further discussed later, analyzing the flame structures.

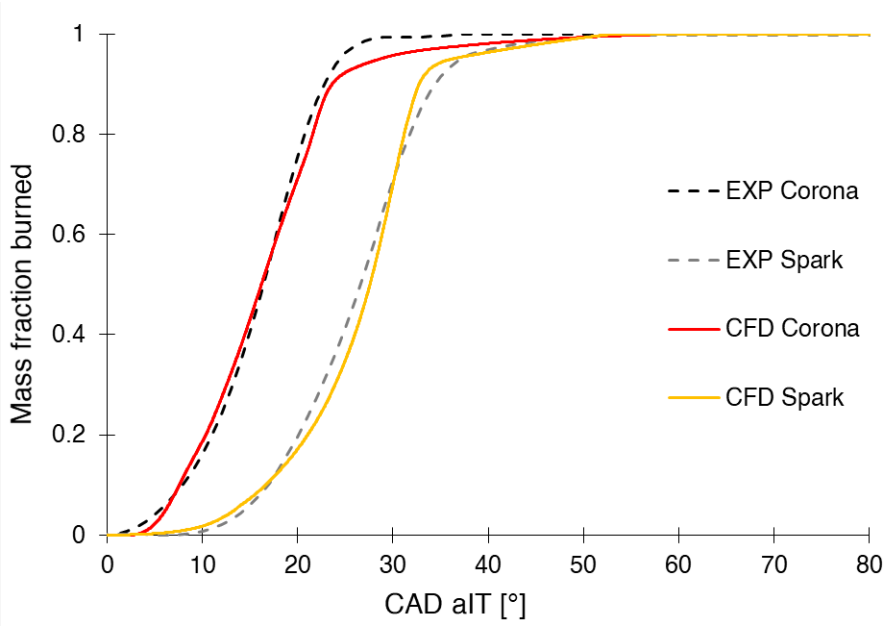

Figure 14. Comparison of MFB for stoichiometric combustion with spark and corona igniter.

To get more persuasive conclusions about the robustness of the RANS model, the CA1, i.e. CA_{MFB1}-CA_{spark} (corresponding to an equivalent average flame radius value of about 9 mm) has been analyzed, comparing the current numerical results with previous engine tests reported in Cimarello et al. [57]. Predictions shown in Figure 15.a confirm that the corona ignition is about four times faster than the spark in reaching the CA1 in all the operating conditions, due to the volumetric ignition effect assisted by the presence of active radicals.

From the simulation point of view, the most remarkable result that can be observed, however, is the ability of the model to predict a change in the CA1 vs. λ curves at the lean limit, as observed in the engine measurements. The lean limit, as shown in Figure 15.b, is actually determined by the sudden rise of the coefficient of variation of the indicated mean effective pressure (COV of IMEP) vs. the relative air-fuel ratio, denoting that combustion instabilities kicks in. This knee point is reflected in the CA1 curves too. The combustion becomes unstable after that point, where large cycle-to-cycle variabilities are observed. The RANS-based model is not meant for capturing such phenomena related to turbulent fluctuations, but the behavior of the average combustion duration is still predicted (Figure 15.a). This suggests that the fundamental aspects underlying the corona ignition process, relevant to SI engine applications, are correctly captured and included in the proposed RANS model.

From the above discussion, the most important aspects for the prediction accuracy of the corona ignition can be summarized in the necessity for (1) an adequate geometrical representation of the streamer plasma channels and for (2) the quantitative estimation of atomic oxygen.

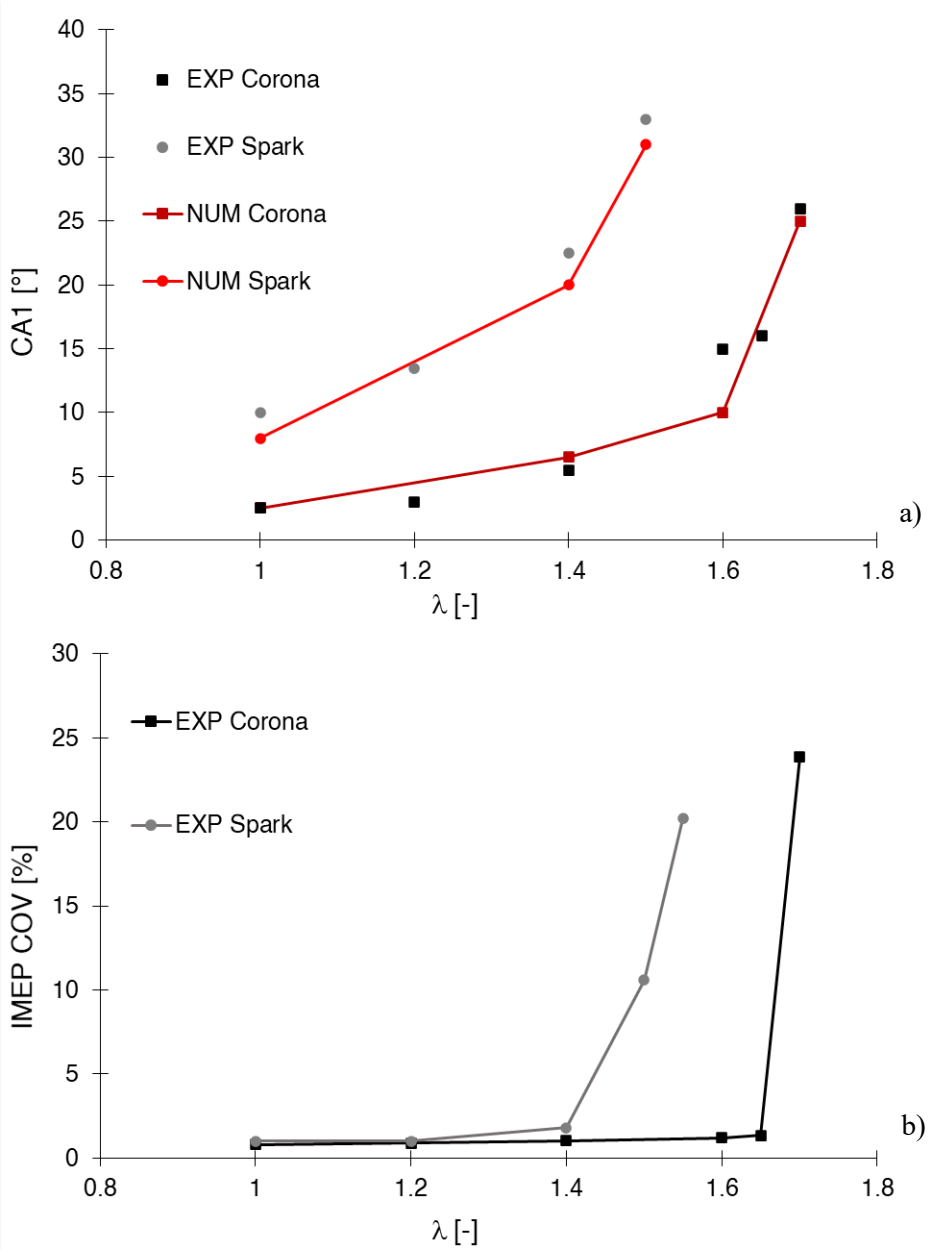

Figure 15. Crank angle interval from the ignition to 1% MFB (flame eq. radius value of 9 mm) (a) and IMEP coefficient of variation (b) as a function of λ.

Comparison between spark and corona ignition – Flame structure

The maximum influence of the corona ignition is in the early stage of the combustion. As visible in Figure 4, the flame kernel generated by the spark ignition is confined in the small region between the electrodes, and therefore the flame needs time to expand and grow in the combustion chamber. On the contrary, the corona discharge involves immediately a wide volume, the flame surface area is considerably larger, and the propagation inside the combustion chamber takes place very rapidly.

Optical data can be particularly useful to investigate the flame kernel formation and the initial combustion development. A detailed analysis of the flame structure is provided in Figure 16 and Figure 17, by comparing the experimental and numerical flames at different timings, observed from the same bottom view. Figure 16 refers to

stoichiometric conditions, while Figure 17 to lean conditions at $\lambda = 1.4$. Since the high-speed camera captures the natural flame luminosity of the whole flame converting it to a 12-bit-depth grayscale, to have a better visual comparison the simulated flame is shown creating the volumetric rendering of the temperature field, with the color code in the range 1200-2200 K [69]. Five different timings are reported and compared. The red circles mark the edge of the optical access. The spark-ignited flame grows gradually and slowly, as expected. The corona-ignited flame develops very quickly to a large enflamed area. The four streamers generate lobes which eventually merge into a single flame. For the $\lambda = 1.0$ case, the flame produced by the spark starts to expand outside of the electrode region 8 CAD after ignition, while at the same time instant, the flame generated by the corona is much larger and about to reach the optical access limit. For the $\lambda = 1.4$ lean case, the flame produced by the corona reaches the optical access limit 12 CAD after the ignition, when the flame generated by the spark is still confined between the electrodes; only 16 CAD after the ignition, the spark-generated flame starts to penetrate into the main chamber. In all cases, the flames slightly move towards the exhaust valves due to a slight bulk charge motion. Another notable feature is that the main expansion is along the chamber roof edge, which is expected because of the larger volume present in this direction.

Overall, RANS simulations are able to reproduce the marked differences in the early flame kernel growth observed in experimental images. This simulation approach is proved to be a viable tool for studying and optimizing SI engines by applying advanced ignition systems, like the corona discharge igniter which generates a non-equilibrium plasma.

Spark		Corona		
Experiments	Simulations	Experiments	Simulations	Timing
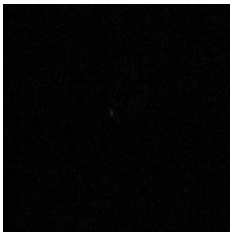	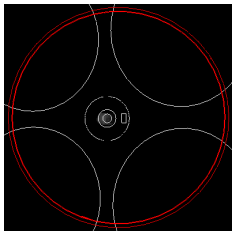	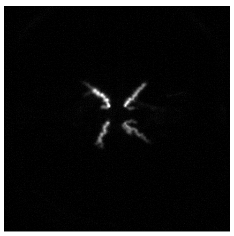	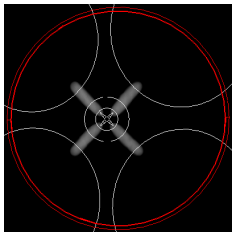	1 CAD aIT
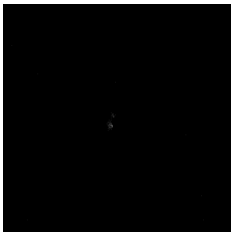	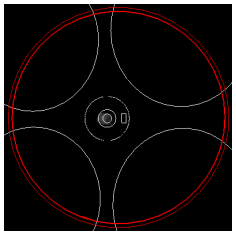	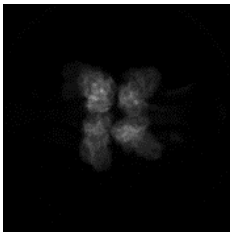	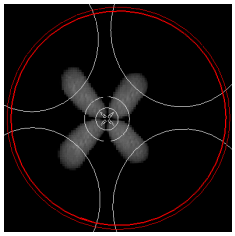	4 CAD aIT
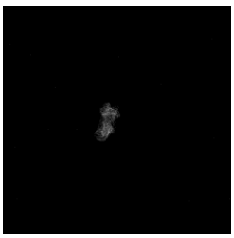	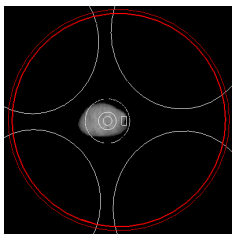	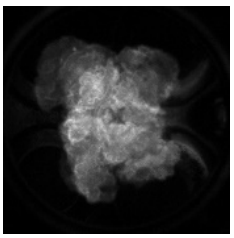	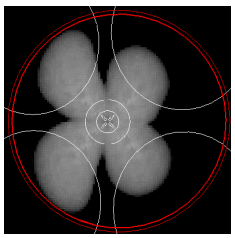	8 CAD aIT
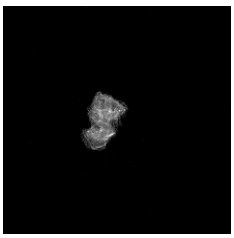	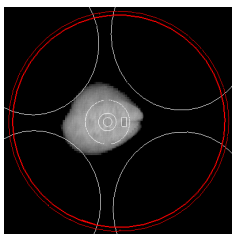	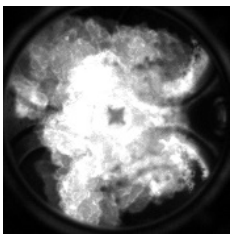	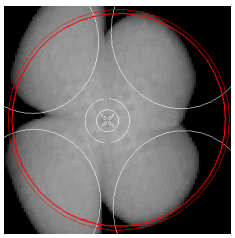	12 CAD aIT
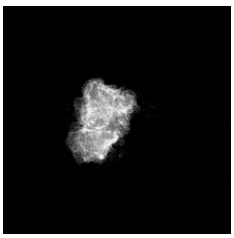	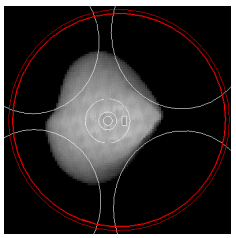	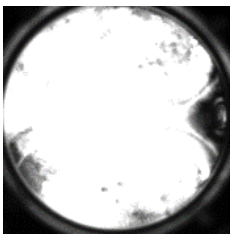	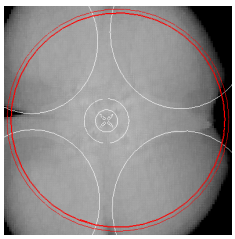	16 CAD aIT

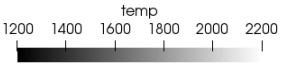

Figure 16. Flame front images comparison in stoichiometric conditions (λ = 1.0). Crank angles are given after ignition timing.

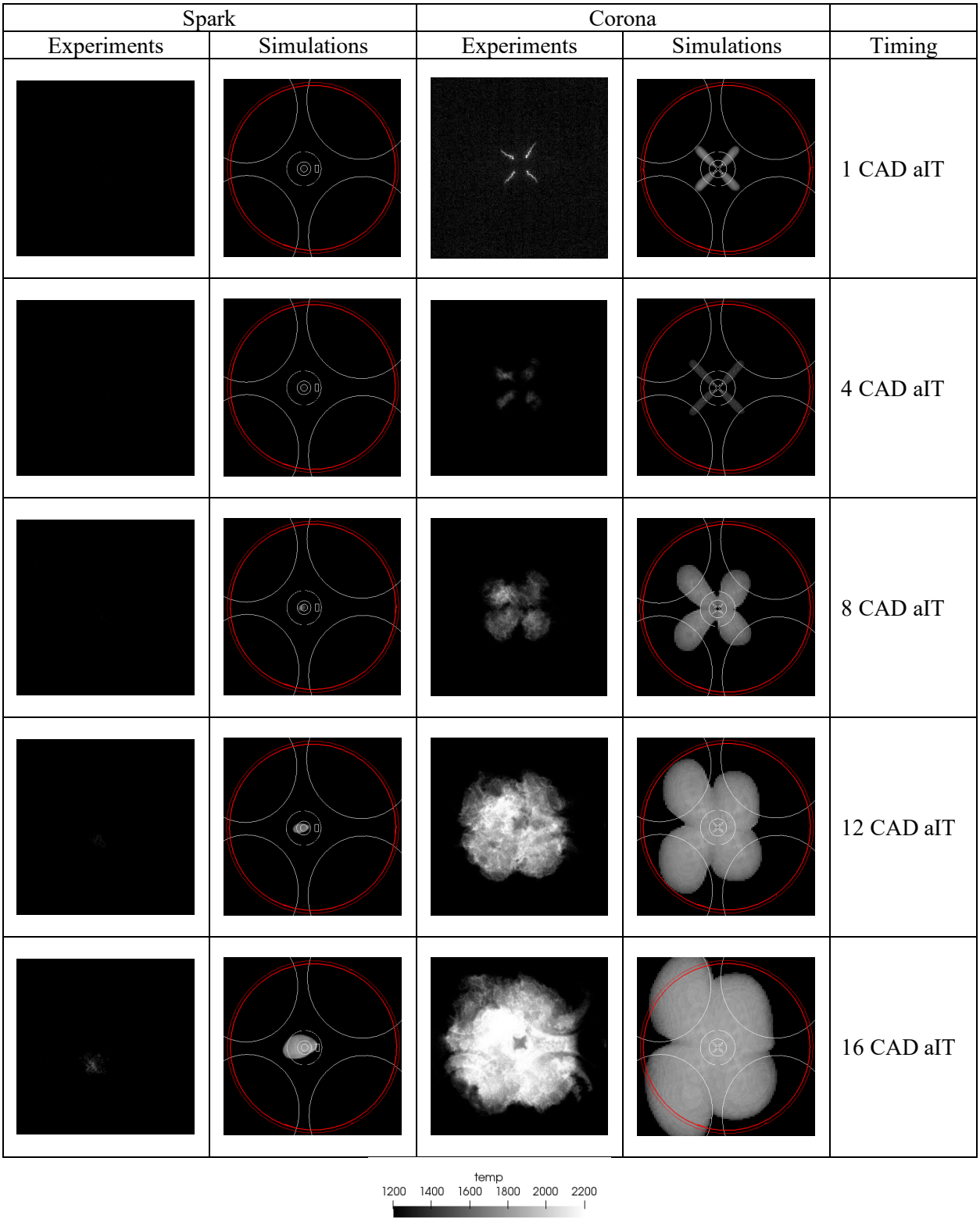

Figure 17. Flame front images comparison in lean conditions (λ = 1.4). Crank angles are given after ignition timing.

CONCLUSIONS

The study analyzes the combustion behavior of a corona ignited flame compared to a standard spark ignited process, in an optically accessible SI engine, by means of RANS simulations. The corona discharge produces a non-equilibrium and low-temperature plasma, that involves a large ignition volume through the streamers. Conversely, the spark discharge produces a thermal plasma localized in a small ignition volume. Simulations are compared with optical engine data, at various AFRs, in order assess the effect of the mixture compositions. The main findings related to this work are listed below:

1. Investigations on the effect of active radicals deposition (atomic oxygen) reveal that the initial combustion development and therefore the peak local temperature is highly dependent on the discharge type.
    - The combustion rate obtained with the spark is unaffected by the presence of active radicals, since the local temperatures reached exceed 10,000 K, typical of a thermal plasma.
    - By contrast, the speed-up effect on the kernel growth and initial combustion stage obtained with the corona igniter is due to the presence of atomic oxygen, within a relatively low-temperature plasma, that remains below 3000 K.
2. The chemical kinetics model for the combustion is able to properly consider the effect originated from radical deposition, successfully replicating the experimental corona ignition behavior. The atomic oxygen mainly affects the early combustion stage, since it reduces the ignition delay timing, confirming that radicals are promoters of the ignition and transition to stable flame. This effect is amplified with lean mixtures.
3. Simulations confirm that corona ignition is about four time faster in reaching the 1% MFB in all the operating conditions, as shown by experimental data, due to the large volume of mixture involved in the discharge and thanks to the radical production.
4. The combustion evolution of the corona ignited flame vs. the spark ignited flame, is markedly different. Validated CFD results allow to identify the main controlling factors, specifically the role of active radicals and of the volumetric ignition sources produced by corona streamers.

Further works will investigate possible improvements and analyses, with the possibility of performing LES simulations to analyze and compare the cycle-to-cycle variability produced by the spark and the corona igniter.

ACKNOWLEDGMENTS

The computational resources provided by the Italian Cineca consortium under the Iscra initiative - awards openPG19 and SimRFmix HP10CEH3NA, 2019-2020 - on the supercomputer Marconi are acknowledged.

Argonne National Laboratory's work was supported by the U.S. Department of Energy, Office of Vehicle Technologies (VTO), under contract DE-AC02-06CH11357.

NOMENCLATURE

ACIS	Advanced Corona Ignition System
AFR	Air-Fuel Ratio
AMR	Adaptive Meshing Refinement
aTDC	After Top Dead Center
bTDC	Before Top Dead Center
CA1	Crank Angle Interval between ignition timing and MFB 1%
CA10	Crank Angle Interval between ignition timing and MFB 10%
CA20	Crank Angle Interval between ignition timing and MFB 20%
CAD	Crank Angle Degree

CCV	Cycle-to-Cycle Variability
CFD	Computational Fluid Dynamics
DI	Direct Injection
ECU	Engine Control Unit
EGR	Exhaust Gas Recirculation
GDI	Gasoline Direct Injection
ICE	Internal Combustion Engine
MBT	Maximum Brake Torque timing
MFB	Mass Fraction Burned
MON	Motor Octane Number
PFI	Port Fuel Injection
PISO	Pressure Implicit with Splitting of Operators
PRF	Primary Reference Fuel
PSR	Perfectly Stirred Reactor
RANS	Reynolds Averaged Navier-Stokes
RF	Radio-Frequency
RON	Research Octane Number
RPM	Revolutions Per Minute
SI	Spark Ignition
λ	Relative Air-Fuel Ratio

APPENDIX

Figure A 1 shows the laminar flame speed enhancement with atomic oxygen addition as a function of the equivalent ratio. The results are obtained from 1D laminar premixed flame calculations at 101325 Pa and 300 K, using a gasoline surrogate constituting of 95% iso-octane and 5% n-heptane by volume. The laminar flame speed is substantially enhanced, with the larger effects for very lean or rich equivalence ratios. Specifically, this enhancement ranges from 10% to 15% when an atomic oxygen concentration of 8000 ppm is used. This concentration corresponds to the generation rate of 3.9 mg/s of O in the streamer volume observed in [67] and leading to the mass reported in Table 4. Specific data for validation, regarding gasoline fuel and atomic oxygen radical, are not available in the literature, but the trend shown in Figure A 1 is very similar to what is reported for lighter hydrocarbons, like propane and methane, with O_3 addition [78 - 80], under equivalent O ppm seeding.

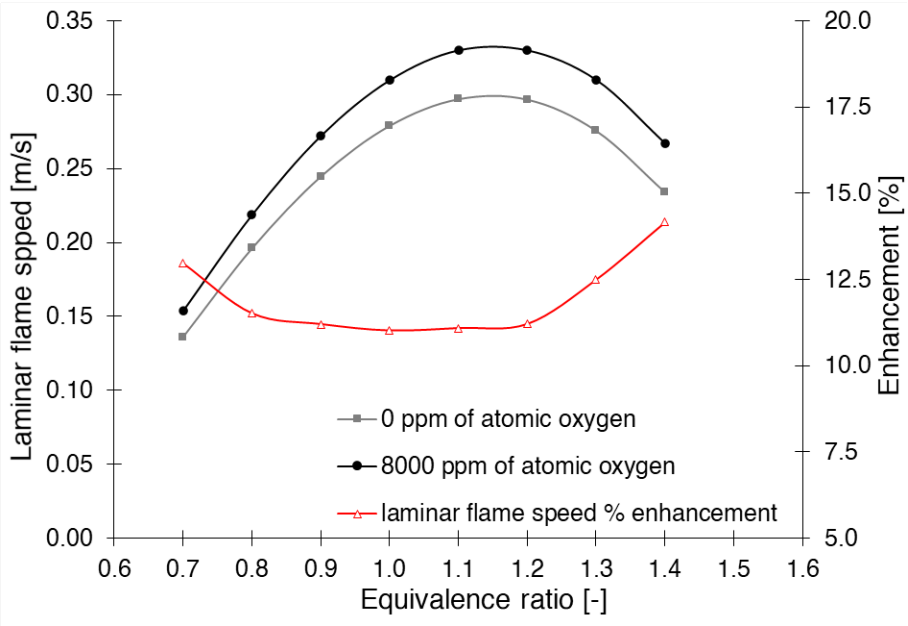

Figure A 1. Effect of atomic oxygen addition on laminar flame speed.

REFERENCES

1. Aleiferis, P.G., Taylor, A.M.K.P., Ishii, K., and Urata, Y., "The Nature of Early Flame Development in a Lean-Burn Stratified-Charge Spark-Ignition Engine," *Combustion and Flame* 136(3):283-302, 2004, doi:10.1016/j combust flame.2003.08.011.
2. Battistoni, M., Poggiani, C., and Grimaldi, C.N., "Experimental Investigation of a Port Fuel Injected Spark Ignition Engine Fuelled with Variable Mixtures of Hydrogen and Methane," *SAE Technical Paper (2013-01-0226)*, 2013, doi:10.4271/2013-01-0226.
3. Alvarez, C.E.C., Couto, G.E., Roso, V.R., et al. "A review of prechamber ignition systems as lean combustion technology for SI engines," *Applied Thermal Engineering* 128 (2018) 107-120, doi: https://doi.org/10.1016/j.applthermaleng.2017.08.118.
4. Santos, N.D.S.A., Alvarez, C.E.C., Roso, V.R., Baeta, J.G.C., and Valle, R.M., "Combustion analysis of a SI engine with stratified and homogeneous pre-chamber ignition system using ethanol and hydrogen," *Applied Thermal Engineering* 160 (2019) 113985, doi:10.1016/j.applthermaleng.2019.113985
5. Wei, H., Zhu, T., Shu, G., Tan, L. et al., "Gasoline Engine Exhaust Gas Recirculation - A Review," *Applied Energy* 99:534-544, 2012, doi:10.1016/j.apenergy.2012.05.011.
6. Galloni, E., Fontana, G., and Palmaccio, R., "Numerical analyses of EGR techniques in a turbocharged spark-ignition," *Applied Thermal Engineering* 39 (2012) 95-104, doi: https://doi.org/10.1016/j.applthermaleng.2012.01.040.
7. Salvi, B.L. and Subramanian, K.A., "Experimental investigation on effects of exhaust gas recirculation on flame kernel growth rate in a hydrogen fuelled spark ignition engine," *Applied Thermal Engineering* 107 (201) 48–54, doi:10.1016/j.applthermaleng.2016.06.125.
8. Battistoni, M.; Grimaldi, C.; Cruccolini, V.; Discepoli, G.; De Cesare, M. "Assessment of Port Water Injection Strategies to Control Knock in a GDI Engine through Multi-Cycle CFD Simulations" *SAE Technical Paper* 2017-24-0034; SAE International: Warrendale, PA, USA, 2017.
9. Zembi J, Battistoni M, Ranuzzi F, Cavina N, De Cesare M. "CFD analysis of port water injection in a GDI engine under incipient knock conditions" *Energies* 2019;12(18):3409. https://doi.org/10.3390/en12183409
10. Goldwitz, J.A. and Heywood, J.B., "Combustion Optimization in a Hydrogen-Enhanced Lean-Burn SI Engine," *SAE Technical Paper (2005-01-0251)*, 2005, doi:10.4271/2005-01-0251.

11. Yu, X., Wu, H., Du, Y., Tang, Y., Liu, L., and Niu, R., "Research on cycle-by-cycle variations of an SI engine with hydrogen direct injection under lean burn conditions," *Applied Thermal Engineering* 109 (2016) 569–581, doi:10.1016/j.applthermaleng.2016.08.077.
12. Zhu, L., He, Z.Y., Xu, Z., et al. "Improving cold start, combustion and emission characteristics of a lean burn spark ignition natural gas engine with multi-point hydrogen injection," *Applied Thermal Engineering* 121 (2017) 83-89, doi:https://doi.org/10.1016/j.applthermaleng.2017.04.023.
13. Heywood, J.B., "*Internal Combustion Engine Fundamentals*," McGraw-Hill, ISBN 0-07-028637-X, 1988.
14. Kalghatgi, G., "Is it really the end of internal combustion engines and petroleum in transport?," *Applied Energy* 225(February):965–974, 2018, doi:10.1016/j.apenergy.2018.05.076
15. Poggiani, C., Cimarello, A., Battistoni, M., Grimaldi, C.N., Dal Re, M. a., and Cesare, M.D., "Optical Investigations on a Multiple Spark Ignition System for Lean Engine Operation," *SAE Technical Paper (2016-01-0711)*, ISBN 2016010711, 2016, doi:10.4271/2016-01-0711.
16. Poggiani, C., Battistoni, M., Grimaldi, C., and Magherini, A., "Experimental Characterization of a Multiple Spark Ignition System," *Energy Procedia* 82:89-95, 2015, doi:10.1016/j. egypro.2015.11.887.
17. Jung, D. and Iida, N., "An investigation of multiple spark discharge using multi-coil ignition system for improving thermal efficiency of lean SI engine operation," *Applied Energy* 212(September 2017):322–332, 2018, doi:10.1016/j.apenergy.2017.12.032.
18. Alger, T., Gingrich, J., Roberts, C., and Mangold, B., "A High Energy Continuous Discharge Ignition System for Dilute Engine Applications," *SAE Technical Paper (2013-01-1628)*, 2013, doi:10.4271/2013-01-1628.
19. Dale, J.D., Checkel, M.D., and Smy, P.R., "Application of High Energy Ignition Systems to Engines," *Progress in Energy and Combustion Science* 23:379-398, 1997, doi:10.1016/S03601285(97)00011-7.
20. Tsuboi, S., Miyokawa, S., Matsuda, M., Yokomori, T., and Iida, N., "Influence of spark discharge characteristics on ignition and combustion process and the lean operation limit in a spark ignition engine," *Applied Energy* 250(January):617–632, 2019, doi:10.1016/j.apenergy.2019.05.036.
21. Chen, L., Wei, H., Zhang, R., et al. "Effects of spark plug type and ignition energy on combustion performance in an optical SI engine fueled with methane," *Applied Thermal Engineering* 148 (2019) 188-195, doi: https://doi.org/10.1016/j.applthermaleng.2018.11.052.
22. Tolou S, Schock H. Experiments and modeling of a dual-mode, turbulent jet ignition engine. *International Journal of Engine Research* 2020, 21(6), 966-986. DOI: https://doi.org/10.1177/1468087419875880.
23. Chinnathambi P, Thelen B, Cook D, Toulson E. Performance metrics for fueled and unfueled turbulent jet igniters in a rapid compression machine. *Applied Thermal Engineering*, Volume 182, 2021, 115893. DOI: https://doi.org/10.1016/j.applthermaleng.2020.115893.
24. Desantes JM, López JJ, Novella R, et al. Pre-chamber ignition systems: A methodological proposal to reproduce a reference case in a simplified experimental facility for fundamental studies. *International Journal of Engine Research*, November 2020. DOI: https://doi.org/10.1177/1468087420971115.
25. Starikovskiy, A., Aleksandrov N., "Plasma-assisted ignition and combustion", *Progress in Energy and Combustion Science* 39 (2013) 61–110.
26. Merola, S.S., Marchitto, L., Tornatore, C., Valentino, G., and Irimescu, A., "Optical characterization of combustion processes in a DISI engine equipped with plasma-assisted ignition system," *Applied Thermal Engineering* 69 (2014) 177–187, doi:10.1016/j.applthermaleng.2014.04.046.
27. Hwang, J., Kim, W., Bae, C., Choe, W., Cha, J., and Woo, S., "Application of a novel microwave-assisted plasma ignition system in a direct injection gasoline engine," *Applied Energy* 205(April):562–576, 2017, doi:10.1016/j.apenergy.2017.07.129.
28. Pischinger, S. and Heywood J., "How Heat Losses to the Spark Plug Electrodes Affect Flame Kernel Development in an SI-Engine," *SAE Tech. Pap. 900021*, 1990, doi:10.4271/900021.
29. Sher, E., Ben-Ya'ish, J., Pokryvailo, A., and Spector, Y., "A Corona Spark Plug System for Spark-Ignition Engines," *SAE Technical Paper 920810*, 1992, doi:10.4271/920810.
30. Varma, A.R. and Thomas, S., "Simulation, Design and Development of a High Frequency Corona Discharge Ignition System," *SAE Technical Paper (2013-26-0014)*, 2013, doi:10.4271/2013-26-0014.

31. Burrows, J., Mixell, K., Reinicke, P.B., Riess, M., Sens, M., "Corona Ignition - Assessment of Physical Effects by Pressure Chamber, Rapid Compression Machine, and Single Cylinder Engine Testing," *2nd International Conference on Ignition Systems for Gasoline Engines*, 2014.
32. Mariani, A. and Foucher, F., "Radio Frequency Spark Plug: An Ignition System for Modern Internal Combustion Engines," *Applied Energy* 122:151-161, 2014, doi:10.1016/j.apenergy.2014.02.009.
33. Domingues, E., Burey, M., Lecordier, B., and Vervisch, P., "Ignition in an SI Engine using Nanosecond Discharges generated by a Spark Gap Plasma Igniter (SGPI)," *SAE Technical Paper (2008-01-1628)*, 2008, doi:10.4271/2008-01- 1628.
34. Yu, J., He, L., Ding, W., et al. "Research on the impacts of air temperature on the evolution of nanosecond pulse discharge products,", *Applied Thermal Engineering* 98 (2016) 265-270, doi: https://doi.org/10.1016/j.applthermaleng.2015.12.013.
35. Shiraishi, T., Urushihara, T., and Gundersen, M., "A Trial of Ignition Innovation of Gasoline Engine by Nanosecond Pulsed Low Temperature Plasma Ignition," *Journal of Physics D: Applied Physics* 42(13):135208, 2009, doi:10.1088/0022-3727/42/13/135208.
36. Starikovskii, A.Y., Anikin, N.B., Kosarev, I.N., Mintoussov, E.I. et al., "Nanosecond-Pulsed Discharges for Plasma- Assisted Combustion and Aerodynamics," *Journal of Propulsion and Power* 24(6):1182-1197, 2008, doi:10.2514/1.24576.
37. Sevik, J., Wallner, T., Pamminger, M., Scarcelli, R., Singleton, D., and Sanders, J., "Extending Lean and Exhaust Gas Recirculation-Dilute Operating Limits of a Modern Gasoline Direct-Injection Engine Using a Low-Energy Transient Plasma Ignition System," *Journal of Engineering for Gas Turbines and Power* 138(11):112807, 2016, doi:10.1115/1.4033470.
38. Shiraishi, T., "Fundamental Analysis of Combustion Initiation Characteristics of Low Temperature Plasma Ignition for Internal Combustion Gasoline Engine," *SAE Technical Paper (2011-01-0660)*, 2018, doi:10.4271/2011-01-0660.
39. Ikeda, Y., Padala, S., Makita, M., and Nishiyama, A., "Development of Innovative Microwave Plasma Ignition System with Compact Microwave Discharge Igniter," *SAE Technical Paper (2015-24-2434)*, 2015, doi:10.4271/2015-24-2434.
40. Nishiyama, A. and Ikeda, Y., "Improvement of Lean Limit and Fuel Consumption Using Microwave Plasma Ignition Technology," *SAE Technical Paper (2012-01-1139)*, 2012, doi:10.4271/2012-01-1139.
41. DeFilippo, A. et al., "Extending the Lean Stability Limits of Gasoline Using a Microwave-Assisted Spark Plug," 1, 2011, doi:10.4271/2011-01-0663.
42. Padala, S., Nagaraja, S., Ikeda, Y., and Le, M.K., "Extension of Dilution Limit in Propane-Air Mixtures Using Microwave Discharge Igniter," in *13th Int. Conf. Engines Veh.*, X, 2017, doi:10.4271/2017-24-0150.
43. Idicheria, C.A., Yun, H., and Najt, P.M., "An Advanced Ignition System for High Efficiency Engines," in *Ignition Systems for Gasoline Engines: 4th International Conference, December 6 - 7, 2018, Berlin, Germany, 2018*, 40-54, doi:10.5445/IR/1000088317.
44. Cruccolini, V., Discepoli, G., Ricci, F., Petrucci, L. et al., "Comparative Analysis between a Barrier Discharge Igniter and a Streamer-Type Radio-Frequency Corona Igniter in an Optically Accessible Engine in Lean Operating Conditions," *SAE Technical Paper (2020-01-0276)*, 2020, https://doi.org/10.4271/2020-01-0276.
45. Breden, D., Idicheria, C.A., Keum, S., Najt, P.M., and Raja, L.L., "Modeling of a Dielectric-Barrier Discharge-Based Cold Plasma Combustion Ignition System," *IEEE Transactions on Plasma Science PP(99):1-9*, DOI: 10.1109/TPS.2018.2882830.
46. Starikovskaia, S.M., "Plasma Assisted Ignition and Combustion," *Journal of Physics D: Applied Physics* 39(16):R265-R299, 2006, doi:10.1088/0022-3727/39/16/R01.
47. Ju, Y. and Sun, W., "Plasma Assisted Combustion: Dynamics and Chemistry," *Progress in Energy and Combustion Science* 48:21-83, 2015, doi:10.1016/j.pecs.2014.12.002.
48. Ju, Y. and Sun, W., "Plasma Assisted Combustion: Progress, Challenges, and Opportunities," *Combustion and Flame* 162(3):529-532, 2015, doi:10.1016/j.combustflame.2015.01.017.
49. Kalman, H. and Sher, E., "Enhancement of heat transfer by means of a corona wind created by a wire electrode and confined wings assembly," *Applied Thermal Engineering* 21 (2001) 265–282, doi:10.1016/S1359-4311(00)00038-7.

50. Wang, F., Liu, J.B., Sinibaldi, J., Brophy, C. et al., "Transient plasma ignition of quiescent and flowing air/fuel mixtures," *IEEE Trans. Plasma Sci* 33(2 II):844-849, 2005, doi:10.1109/ TPS.2005.845251.
51. Yu, S., Wang, M., and Zheng, M., "Distributed Electrical Discharge to Improve the Ignition of Premixed Quiescent and Turbulent Mixtures," *SAE Technical Paper (2016-01- 0706)*, 2016, doi:10.4271/2016-01-0706.
52. Pineda, D.I., Wolk, B., Chen, J.-Y., and Dibble, R.W., "Application of Corona Discharge Ignition in a Boosted Direct-Injection Single Cylinder Gasoline Engine: Effects on Combustion Phasing, Fuel Consumption, and Emissions," *SAE Int. J. Engines* 9(3):1970-1988, 2016, doi:10.4271/2016-01-9045.
53. Schenk, M., Schauer, F.X., Sauer, C., Weber, G., Hahn, J., and Schwarz, C., "Challenges to the Ignition System of Future Gasoline Engines - An Application Oriented Systems Comparison," *Ignition Systems for Gasoline Engines*, Springer International Publishing, Cham: 3-25, 2016, doi:10.1007/978-3-319-45504-4_1.
54. Bresler, M., Attard, W., and Reese, R., "Investigation of Alternative Ignition System Impact on External EGR Dilution Tolerance in a Turbocharged Homogeneous Direct Injected Spark Ignited Engine," *SAE Int. J. Engines* 8(4):1967-1976, 2015, doi:10.4271/2015-01-9043.
55. Idicheria, C.A., and Najt, P.M., "Potential of Advanced Corona Ignition System (ACIS) for Future Engine Applications," *Ignition Systems for Gasoline Engines*, Springer International Publishing, Cham, ISBN 978-3-319-45503-7: 315-331, 2017, doi:10.1007/978-3-319-45504-4_19.
56. Marko, F., König, G., Schöffler, T., Bohne, S., and Dinkelacker, F., "Comparative Optical and Thermodynamic Investigations of High Frequency Corona and Spark Ignition on a CV Natural Gas Research Engine Operated with Charge Dilution by Exhaust Gas Recirculation," *Ignition Systems for Gasoline Engines*, Springer International Publishing, Cham, ISBN 978-3-319-45503-7: 293-314, 2017, doi:10.1007/978-3-319-45504-4_18.
57. Cimarello, A., Grimaldi, C.N., Mariani, F., Battistoni, M., and Dal Re, M., "Analysis of RF Corona Ignition in Lean Operating Conditions Using an Optical Access Engine," *SAE Technical Paper, (2017-24-0673)*, 2017, doi:10.4271/2017-01-0673.
58. Cimarello, A., Cruccolini, V., Discepoli, G., Battistoni, M. et al., "Combustion Behavior of an RF Corona Ignition System with Different Control Strategies," *SAE Technical Paper (2018-01-1132)*, 2018, doi:10.4271/2018-01-1132.
59. Cruccolini, V., Discepoli, G., Cimarello, A., Battistoni, M. et al., "Lean combustion analysis using a corona discharge igniter in an optical engine fueled with methane and a hydrogen-methane blend," *Fuel* 259 (2020) 116290, doi: 10.1016/j.fuel.2019.116290.
60. Eichwald O, Ducasse O, Dubois D, Abahazem A, Merbahi N, Benhenni M, et al., "Experimental analysis and modelling of positive streamer in air: towards an estimation of O and N radical production," *J Phys D Appl Phys* 2008;41:234002. doi:10.1088/0022-3727/41/23/234002.
61. Qin J, Pasko VP, "On the propagation of streamers in electrical discharges," *J Phys D Appl Phys* 2014;47:435202. doi:10.1088/0022-3727/47/43/435202.
62. Bagheri B, Teunissen J, Ebert U, Becker MM, Chen S, Ducasse O, et al, "Comparison of six simulation codes for positive streamers in air," *Plasma Sources Sci Technol* 2018;27:095002. doi:10.1088/1361-6595/aad768.
63. Scarcelli, R., Zhang, A., Wallner, T., Breden, D. et al., "Multi-dimensional Modeling of Non-equilibrium Plasma for Automotive Applications," SAE Technical Paper 2018-01-0198, 2018, doi:10.4271/2018-01-0198.
64. Scarcelli, R., Wallner, T., Som, S., Biswas, S., Ekoto, I., Breden, D., Karpatne, A., and Raja, L.L., "Modeling non-equilibrium discharge and validating transient plasma characteristics at above-atmospheric pressure," Plasma Sources Science and Technology, Volume 27, Number 12, https://doi.org/10.1088/1361-6595/aaf539.
65. Zhang, A., Scarcelli, R., Wallner, T., Breden, D., Karpatne, A., Raja, L.L., Ekoto, I., and Wolk, B., "Numerical Investigation of Nanosecond Pulsed Discharge in Air at Above-Atmospheric Pressures," *Journal of Physics D Applied Physics* 51(34), DOI: 10.1088/1361-6463/aad262.
66. Wolk, B., and Ekoto, I., "Calorimetry and Imaging of Plasma Produced by a Pulsed Nanosecond Discharge Igniter in EGR Gases at Engine-Relevant Densities," *SAE Int. J. Engines* 10(3):970-983, 2017, https://doi.org/10.4271/2017-01-0674.
67. Cruccolini, V., Scarcelli, R., Battistoni, M., Grimaldi, C.N., Dal Re, M., Breden, D., Raja, L.L, "Multidimensional modeling of non-equilibrium plasma generated by a radio-frequency corona discharge," *Plasma Sources Science and Technology,* 2020, 29 115013. DOI: 10.1088/1361-6595/abb938.

68. Ricci, F., Zembi, J., Battistoni, M., Grimaldi, C. et al., "Experimental and Numerical Investigations of the Early Flame Development Produced by a Corona Igniter," *SAE Technical Paper (2019-24-0231)*, 2019, doi:10.4271/2019-24-0231.
69. Zembi, J., Mariani, F., and Battistoni, M., "Large Eddy Simulation of Ignition and Combustion Stability in a Lean SI Optical Access Engine," SAE Technical Paper (2019-24-0087), 2019, doi:10.4271/2019-24-0087.
70. Battistoni, M., Mariani, F., Risi, F., and Poggiani, C., "Combustion CFD Modeling of a Spark Ignited Optical Access Engine Fueled with Gasoline and Ethanol," *Energy Procedia* 82:424-431, 2015.
71. Donadio, G., Poggiani, C., Rondoni, L., Grimaldi, C.N. et al., "Combustion Analysis in an Optical Access Engine," *Energy Procedia* 45:959-966, 2014.
72. Richards, K.J., Senecal, P.K., and Pomraning, E., "CONVERGE v.3.0 Documentation," Convergent Sciences Inc., 2020.
73. Senecal, P., Richards, K., Pomraning, E., Yang, T. et al., "A New Parallel Cut-Cell Cartesian CFD Code for Rapid Grid Generation Applied to in-Cylinder Diesel Engine Simulations," *SAE Technical Paper (2007-01-0159)*, 2007, doi:10.4271/2007-01-0159.
74. Issa, R.I., "Solution of the Implicitly Discretised Fluid Flow Equations by Operator-Splitting," *Journal of Computational Physics, 62(1)*, 40-65, 1986. DOI: 10.1016/0021-9991(86)90099-9.
75. Liu, Y., Jia, M., Xie, M., and Pang, B., "Enhancement of a Skeletal Kinetic Model for Primary Reference Fuel Oxidation by Using a Semidecoupling Methodology," *Energy Fuels* 26(12):7069-7083, 2012.
76. Discepoli, G., Cruccolini, V., Dal Re, M., Zembi, J. et al., "Experimental Assessment of Spark and Corona Igniters Energy Release," *Energy Procedia* 148:1262-1269, 2018.
77. Discepoli, G., Cruccolini, V., Ricci, F., Di Giuseppe, A. et al., "Experimental characterisation of the thermal energy released by a Radio-Frequency Corona Igniter in nitrogen and air," *Applied Energy* 263 (2020) 114617, DOI: 10.1016/j.apenergy.2020.114617.
78. Ombrello, T., Won, S.H., Ju, Y., Williams, S., "Flame propagation enhancement by plasma excitation of oxygen. Part I: Effects of O3," *Combustion and Flame* 157 (2010) 1906–1915, DOI: 10.1016/J.COMBUSTFLAME.2010.02.005.
79. Ombrello, T., Won, S.H., Ju, Y., Williams, S., "Flame propagation enhancement by plasma excitation of oxygen. Part II: Effects of O2($a^1\Delta g$)," *Combustion and Flame* 157 (2010) 1916–1928, DOI: 10.1016/J.COMBUSTFLAME.2010.02.004.
80. Gao, X., Zhang, Y., Adusumilli, S., Seitzman, J., et al., "The effect of ozone addition on laminar flame speed," *Combustion and Flame* 162 (2015) 3914–3924, DOI: 10.1016/j.combustflame.2015.07.028.